Title

MASS AND ORIENTATION EFFECTS IN DISSOCIATIVE COLLISIONS BETWEEN BARE GAS ATOMS AND ALKALI HALIDE MOLECULES

Author

Tully, F.P.

Publication Date

1980-05-01

LBL-10863 c.2
Preprint

Lawrence Berkeley Laboratory
UNIVERSITY OF CALIFORNIA

Materials & Molecular Research Division

Submitted to the Journal of Chemical Physics

MASS AND ORIENTATION EFFECTS IN DISSOCIATIVE COLLISIONS BETWEEN RARE GAS ATOMS AND ALKALI HALIDE MOLECULES

F. P. Tully, N. H. Cheung, H. Haberland, and Y. T. Lee

May 1980

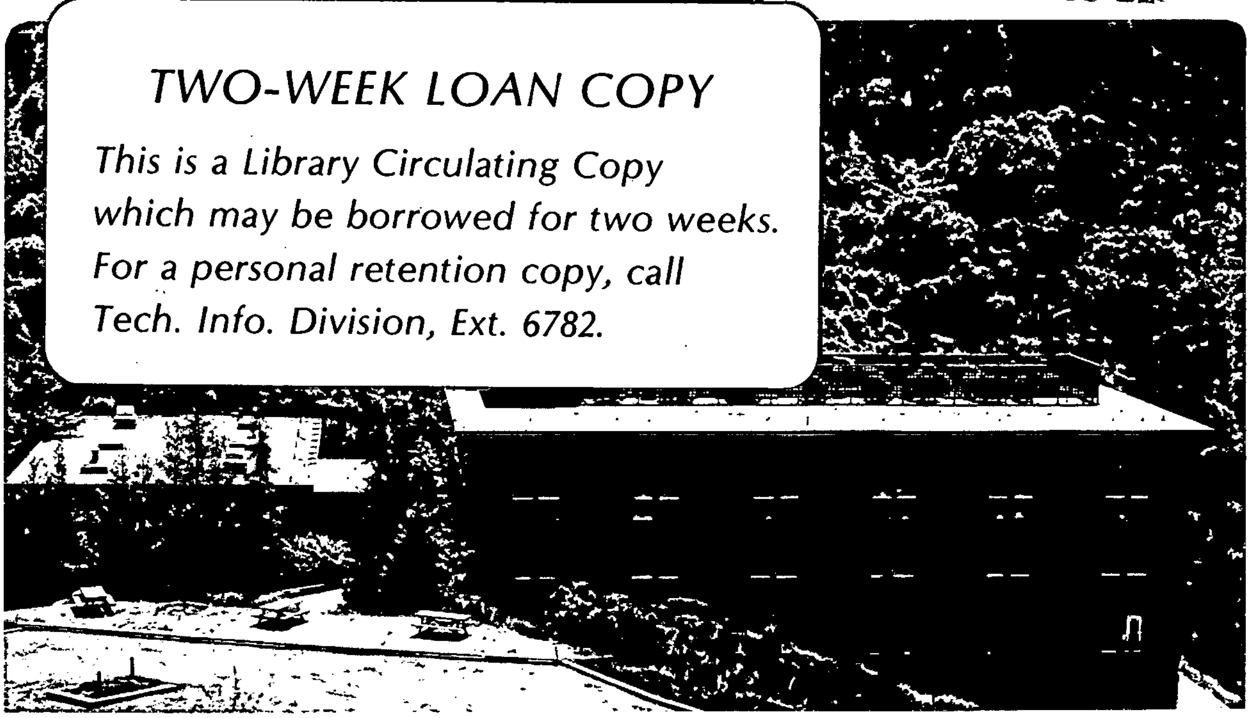

Prepared for the U.S. Department of Energy under Contract W-7405-ENG-48

DISCLAIMER

MASS AND ORIENTATION EFFECTS IN DISSOCIATIVE COLLISIONS BETWEEN RARE GAS ATOMS AND ALKALI HALIDE MOLECULES

F. P. Tully[a], N. H. Cheung[b], H. Haberland[c]

The James Franck Institute and
Department of Chemistry
The University of Chicago
Chicago, Illinois 60637

Y. T. Lee

The James Franck Institute and
Department of Chemistry
The University of Chicago
Chicago, Illinois 60637
and
Materials and Molecular Research Division[d]
Lawrence Berkeley Laboratory and
Department of Chemistry
University of California
Berkeley, California 94720

ABSTRACT

The collision induced dissociation of alkali halide molecules to ion pairs upon impact with hyperthermal rare gas atoms has been investigated using the crossed molecular beam method. Relative total cross sections for the dissociation of CsI, CsBr, RbI and KI to ion pairs upon collision with xenon and krypton have been measured over a relative collision energy range from threshold to 10 eV and 8 eV, respectively. In addition, complete angular and energy distributions of both dissociated ions from Xe + CsI, CsBr and RbI collisions and from Kr + CsI and CsBr collisions have been obtained at several collision energies within the above energy range. Mass, collision orientation and energy dependence effects observed throughout this work define two limiting case dissociation mechanisms for the

Xe(Kr) + MX → Xe(Kr) + M^+ + X^- processes. The dominant dissociation configuration consists of the rare gas atom incident on the light atom end of the alkali halide molecule in a near collinear collision. The less preferred dissociation mechanism results when the rare gas atom is incident in a near collinear configuration on the heavy atom end of the alkali halide molecule. Experimental measurements of the percentage of energy transfer from 3-particle relative kinetic energy to the relative motion of $M^+ - X^-$ range as high as 95%; these percentage energy transfers correlate well with the predictions of an impulsive collision model. Three-dimensional classical trajectory calculations using realistic interaction potentials have been performed and they verify the dynamical interpretation suggested by the experiments.

INTRODUCTION

The conversion of energy from one form to another during a collision between two molecules is a process which has been of central importance to scientists for a long time. The simplest such event is the inelastic collision of an atom with a diatomic molecule. Translational energy associated with the relative motion of the approaching species can be transformed into vibrational, rotational, or electronic energy of the diatomic, or, if sufficient energy is available, can result in dissociation of the diatomic.

The study of the chemical kinetics of endoergic processes involving neutral reactants has accelerated in recent years. One endoergic process which has been the subject of considerable study is the collision-induced dissociation of metal halides. Shock tube studies[1-8] of alkali halide dissociation have shown that both atomic and ionic products are formed, even though dissociation to ionic products requires more energy. Cesium, rubidium, and potassium salts (except perhaps RbI and KI) dissociate predominantly to ion pairs while lithium and sodium salts (possibly excepting NaCl) dissociate almost exclusively to separated atoms. The actual values of the branching ratios for the different dissociation products remain subject to some question. The crossed molecular beam technique has also been applied to metal halide dissociation. Earlier work[9] in this laboratory investigated the dependence of the dissociation cross section on relative kinetic energy and alkali halide internal energy in xenon-induced dissociations of CsI, CsBr, and RbI. Parks _et al._[10-15] have performed experiments to determine the absolute total cross sections for dissociation of TlF, TlCl, TlBr, TlI, CsCl and their corresponding (M_2X_2) dimers to ion pairs upon impact with fast xenon and krypton (also with argon and SF_6 for CsCl). Levine and his coworkers[16-19] have discussed the experimental results using both near classical approaches to collision theory and a statistical theory without making any specific assumptions about the dynamics of the dissociation process. Fan[20] has performed one-dimensional trajectory calculations to investigate the dependence of the dissociation cross section on vibrational energy. Additional experimental work by Piper et al.[21] investigated the absolute total dissociation cross sections of CsBr upon collision with argon and xenon in a higher relative energy range.

In this paper we report a series of detailed studies aimed at gaining dynamical insight into rare gas atom-alkali halide dissociative collisions. Using crossed molecular beams with well-defined distributions in incident velocity and angle, we have measured relative total cross sections for the dissociation of CsI, CsBr, RbI, and KI to ion pairs upon collision with hyperthermal xenon and krypton over a relative collision energy range from threshold to 10 eV and 8 eV, respectively. In addition, we have measured complete angular and energy distributions of both dissociated ions from Xe + CsI, CsBr, and RbI collisions and from Kr + CsI and CsBr collisions at several relative collision energies within the above range. A partial sample of these differential dissociation contours is included in this work to demonstrate that, in the above encounters, certain collision orientations and mass combinations preferentially lead to dissociation. Finally, in order to understand the effect of mass combinations on the dynamics of dissociation, we have performed classical trajectory calculations on the Xe + CsBr system colliding with a most probable relative energy of 6.0 eV. The results of these calculations are compared with a Xe + CsBr experiment with the same initial conditions in which the peaks of the recoil velocity distributions of all three products (Cs^+, Br^-, and Xe) were found to be centered on the relative velocity vector of the colliding system. The comparison of the calculations with experiment has led to a semiquantitative understanding of the very strong mass effects observed throughout all of our work.

EXPERIMENTAL

The collision-induced dissociation experiments were all performed by crossing at 90° an effusive alkali halide beam and the hyperthermal beam of xenon or krypton produced upon supersonic expansion through a heated nozzle of a mixture of 1% (0.5%) xenon or 1% krypton in 99% (99.5%) hydrogen. Ions produced in the dissociation were either deflected into and collected by a Faraday cup, as in the total dissociation cross section measurements, or allowed to pass through the collision volume and into a rotatable plane field retarding energy analyzer, thereby yielding laboratory energy distributions as a function of laboratory angle. A schematic of the experimental arrangement is shown in Figure 1.

The alkali halide beam source consists of a double oven located in a chamber differentially pumped by a 4-inch diffusion pump to an operating pressure of 5×10^{-6} torr. A lower stainless steel oven heated by alumina-insulated tantalum wire windings maintained the vapor pressure of the alkali halide in the range of 0.1 - 1.0 torr. The vaporized salt then flowed into a resistance heated tantalum tube and effused from a 0.76 x 3.05 mm slit located near the midpoint of the tube. A stainless steel heating block with alumina-insulated tantalum heaters was mounted on the top part of the tantalum tube in order to achieve homogeneous heating along the tube and to maintain a maximum in temperature at the slit. The temperature at the slit was measured with an optical pyrometer. Four water-cooled copper plates with successively smaller openings provided initial collimation and most of the trapping of the salt. The beam was finally collimated to 1.8° FWHM by a heated defining slit employing tantalum windings and a second slit located on the differential pumping chamber wall just before the entrance to the scattering chamber. The alkali halide beam intensity was measured by surface ionization on a tungsten filament.

The seeded supersonic molecular beam technique was used to produce xenon and krypton atoms of sufficient energy to induce the highly endothermic bond breakage in the alkali halides. A mixture of 1% (or 0.5%) xenon or 1% krypton in hydrogen carrier was expanded in supersonic flow through a heated tungsten nozzle with a 0.10 mm hole diameter. The center of the beam was sampled by a conical tungsten skimmer of 0.75 mm diameter and collimated to 2.6° FWHM before entering the scattering chamber. Deflection plates were placed very close to the collimation slit to remove ions and electrons formed when the high energy beam impinged on the metal surface during collimation.

The tungsten nozzle consists of a long inner tube of 4.9 mm diameter and 0.76 mm wall thickness joined to a shorter outer jacket of 7.6 mm diameter and 0.64 mm wall thickness close to the nozzle tip. The resistance-heated circuit extends from the end of the outer jacket through the joining point to the far end of the inner tube. The terminals of the tungsten tube are clamped to water-cooled copper blocks, and the copper block which is connected to the inner tube is fixed to a water-cooled ball-slide mechanism which moves in response to expansion of the tungsten tube as it is heated. Experience taught the need for very extensive water-cooling of all components in the vicinity of the tungsten oven. The highest temperature to which the nozzle has been heated, estimated from a tungsten 5% rhenium-tungsten 26% rhenium thermocouple, is 2500°K.

With a typical nozzle stagnation pressure of 3-4 atm, the differentially pumped nozzle-skimmer and skimmer-collimator chambers were maintained at pressures of 2×10^{-4} torr and 5×10^{-6} torr by 10 inch and 4 inch oil diffusion pumps. For sufficiently high source pressures the isentropic expansion produced xenon (krypton) and hydrogen of the same terminal velocity, given approximately[22] by $v = (\frac{5kT}{\bar{m}})^{1/2}$ where $\bar{m} = x_{Xe(Kr)} m_{Xe(Kr)} + x_{H_2} m_{H_2}$ is the mean mass of the mixture, x and m being the mole fraction and mass of the heavy and hydrogen components. For a mixture of 1% xenon in 99% hydrogen, $\bar{m} = 3.29$ a.m.u. Thus the xenon energy obtained using this seeded mixture, $\frac{5}{2} (\frac{m_{Xe}}{\bar{m}})kT$ is a factor of $\frac{m_{Xe}}{\bar{m}}$ ($\approx$ 40) larger than that which would have been obtained by expanding pure xenon at the same temperature. The hydrogen molecules present in the beam, while at least as fast as the xenon, possessed an energy approximately $\frac{1}{65}$ (ratio m_{H_2}/m_{Xe}) that of the xenon and thus did not have enough energy to contribute to the alkali halide dissociation.

As the nozzle temperature increased, the nozzle stagnation pressure required to achieve complete equalization of the xenon and hydrogen terminal velocities increased to a point at which any attempt to operate at a pressure high enough to insure velocity equalization produced a flow rate from the nozzle far in excess of the pumping capability of the system. Thus with the tungsten oven operated above 1000°C, a typical operating pressure of 3 atm was not high enough to insure equalization of the terminal velocities and the condition $v_{Xe} < (\frac{5kT}{\bar{m}})^{1/2} < V_{H_2}$ existed in most experiments.

Because of this slippage between the xenon and hydrogen terminal velocities, even a precisely known nozzle temperature would not have been sufficient for xenon (krypton) atom energy determination.[23] These fast atom beam energies were, therefore, carefully measured by rotating the retarding field energy analyzer into the xenon (krypton)/hydrogen beam, ionizing the beam species with a crossing electron beam immediately preceding the beam entry into the energy analyzer (see Fig. 1), and obtaining an energy distribution of the ionized species. As shown in Fig. 2, an electron beam of 100-140 eV energy was sufficiently energetic to produce singly, doubly, and triply ionized xenon and singly and doubly ionized krypton. Because of the small mass of the electron, the momentum transfer between the ionizing electron and the heavy atom was negligible and the energy of the neutral atom was very nearly equal to the energy of the ionized species, irrespective of the number of electrons stripped off the atom. In the retarding field, however, doubly and triply charged xenon ions were repelled with twice and three times the force of a singly ionized species of the same energy, and thus these peaks appeared at about $\frac{1}{2}$ and $\frac{1}{3}$ of the energy peak position of Xe^+ in the energy spectrum. Calculating the fast atom energy from $E = 2(\text{Peak } (A^+) - \text{Peak } (A^{++}))$ is advantageous over single peak (A^+ only) analysis because this expression eliminates any energy shift contributions from surface charges and contact potentials, contributions which are not only difficult to measure but not necessarily constant in time. The peaks near zero energy in Fig. 2 are due to ions produced by background gas in the chamber.

Using this type of beam energy analysis, then, the total relative dissociation cross section experiments were performed by measuring the total ion current collected in the Faraday cup as a function of the xenon (krypton) beam energy, maintaining a constant salt flux. The dependence of the xenon (krypton) flux on nozzle condition was measured and the total dissociation cross sections were corrected accordingly.

The differential dissociation cross section measurements were performed by grounding the repeller plate of the Faraday cup, turning off the crossing electron beam preceding the energy analyzer, and allowing the ions formed in the dissociation to enter the retarding field energy analyzer unchanged from their state after dissociation. Measurement of the energy distributions at every 5° in the laboratory of both dissociated ions led, after transformation and approximate averaging, to complete center-of-mass velocity and energy contour maps for the system.

The plane field retarding energy analyzer is made of seven thin stainless steel discs insulated from each other by alumina spacers and aligned by four 1/16" solid alumina rods which are fixed into position relative to a mu-metal shielded mounting can by set screws. The first plate is connected to ground to establish a field free region at the entrance. This entrance lens is followed by three focusing plates, then the retarding plate, and finally, two more focusing plates which provide the initial acceleration toward the electron multiplier to those sufficiently energetic ions that have overcome and passed through the retarding field region of the analyzer. It should be noted that all of these plates are externally floated to the retarding plate so that ions of different energy will experience the same accelerations and decelerations within the analyzer, thus minimizing energy dependent transmission effects. In addition plates 4, 5, and 6, i.e., the retarder and its surrounding plates, have flat gold mesh (80% transmission) spot-welded over their holes to insure the uniformity of the fields in the retarding region, to minimize the lens effects characteristic of flat plates with open holes, and to minimize field penetration from the high voltage on the first dynode of the nearby electron multiplier. The precise transmission characteristics of this energy analyzer as a function of ion energy are not known, but possible variations with energy should be small and should not influence our conclusions.

The energy analysis was performed as follows: a DC voltage on the retarding plate was continuously varied by a variable speed ramp generator. Typical scanning speeds were 1 volt/minute. Superimposed on the DC voltage a sinusoidal AC voltage (80-150 cps) from the reference output of a lock-in amplifier was applied as modulation in order to obtain direct measurement of the differential ion energy distribution by the same lock-in amplifier. The peak-peak reference signal height used was 300 mV when measuring the energy distributions of the dissociated ions, and in the range 50-300 mV when measuring the xenon (krypton) beam energy distributions. The full width half maximum velocity spreads of the Xe and Kr beams ranged from 3-5% in all of the experiments.

DATA ANALYSIS

In order to obtain detailed information about the dynamics of a chemical reaction it is necessary to make measurements which characterize the product states following a single reactive collision. Using crossed molecular beams with well-defined distributions in incident velocity and angle, we have measured angular and energy distributions of the ions produced in the collision-induced dissociation of CsI, CsBr, and RbI. From these differential dissociation cross section measurements knowledge relating to the energy disposal among dissociation products and dissociation probability as a function of collision orientation has been obtained. Ultimately, information concerning the interaction potentials of the collision partners could be extracted from these data.

Since dynamical insight can only be gained by considering the relative motion of the collision partners, our initial goal was to obtain the differential dissociation cross sections of the ion pairs in the center-of-mass coordinate system. As a first step toward this goal it was necessary to convert the measured ion laboratory energy distributions, $P(E, \Theta)$, to laboratory velocity distributions, $I(v, \Theta)$. We have

$$P(E,\ \Theta)dE = I(v,\ \Theta)dv$$

and

$$dE = d(\frac{1}{2}mv^2) = mvdv$$

so that

$$I(v,\ \Theta)\,\alpha\ v \cdot P(E,\ \Theta). \qquad (1)$$

Now, as shown in Fig. 3, if the energies of both beams were perfectly monochromatic, the transformation from the laboratory coordinate system (LAB) to the center-of-mass coordinate system (CM) would be unique and the differential cross sections in these two systems would be related by

$$I_{CM}(u,\ \theta) = \frac{u^2}{v^2}\,I_{LAB}(v,\ \Theta) \qquad (2)$$

where u is the CM recoil velocity measured from the tip of the velocity vector $\vec{c}$ indicating the LAB motion of the center-of-mass of the colliding system, and θ is the CM angle of recoil measured from the relative velocity vector describing the relative motion of the collision partners. However, in these as in all crossed beam experiments, neither beam had a delta-function velocity distribution, and thus a single point $(v,\ \Theta)$ on the LAB surface corresponds to a continuum of points $(u,\ \theta)$ on the CM surface.

Following Entemann[24] and Siska,[25] if averaging over the beam distributions is included, the relationship[26] between $I_{CM}(u,\ \theta)$ and $I_{LAB}(v,\ \Theta)$ is given by

$$I_{LAB}(v,\ \Theta) = \int_0^\infty dv_1 \int_0^\infty dv_2\, n_1(v_1) n_2(v_2) V\, \frac{v^2}{u^2}\, I_{CM}(u,\theta,V)$$

where n_1 and n_2 are number density speed distributions in the beams and V is the relative velocity vector. The typical procedure in making use of this relation has been to replace the integrals by a weighted sum over Newton diagrams and to attempt a separation of variables in the center-of-mass differential cross section:

$$I_{CM}(u,\theta,V) = U(u) \cdot T(\theta) \cdot Y(V).$$

Usually these separated representations are defined by functional forms with variable parameters. There is, however, no a priori reason to expect that $I_{CM}(u,\theta,V)$ should be separable in its variables. In fact, there exists ample experimental evidence[27,28] that in some systems recoil velocity and angle are so strongly coupled that use of the separable variable representation will for no choice of parameters yield good agreement between the calculated and measured $I_{LAB}(v, \Theta)$. In the differential dissociation cross section measurements reported here it can be seen from the high recoil energy forward scattered peaks of the light ions that fairly strong coupling exists between recoil angle and velocity. Furthermore, since many of the measured distributions possess two asymmetric overlapping recoil peaks, it would be difficult even to obtain the best separable variable representations which, once acquired, would still give good agreement with the measured data. Finally, because of the narrow velocity distributions of the seeded heavy atom beam[29-31] and the fact that the fast atom velocity vector is more than ten times larger than that of the alkali halide, the narrow fast atom velocity spread dominates in determining the spread in the center-of-mass vectors and a one Newton diagram LAB → CM transformation should yield fairly accurate CM differential dissociation cross sections. These favorable kinematics have led to our decision to use one Newton diagram LAB → CM transformations.

Combining Eqs. (1) and (2) then, we obtain

$$\frac{I_{CM}(u, \theta)}{u^2} \propto \frac{P_{LAB}(E, \Theta)}{v} \qquad (3)$$

The left side of Eq. (3) contains only CM variables while the right side contains only LAB variables. In fact, since the right side does not depend on a choice of center-of-mass point, it will not introduce any improper distortion of the original lab data. These quantities, which except for multiplication by u^2 are equal to $I_{CM}(u, \theta)$ [$Y(V) = 1$ for monochromatic beams], are the contours displayed in Figs. 5-11.

For those experiments in which differential dissociation cross sections were measured for both ions at a particular collision energy, making the assumption that the peaks in the velocity recoil spectra of the two ions on the (u, θ) surface are associated with the same particular collision process, conservation of momentum yields the required velocity recoil peak position of the (unmeasured) fast atom. Summation of the product recoil energies could then be used in an energy balance equation

$$E_{CM} + E_{MX}^{int} = D_e + E_{M^+} + E_{X^-} + E_{atom}$$

to check energy conservation. Here E_{MX}^{int} is the average internal alkali halide energy, E_{M^+}, E_{X^-} and E_{atom} are the recoil energies of M^+, X^- and the rare gas atom, and D_e is the dissociation energy to the ionic limit. In every case in which the Newton diagram used in the LAB → CM transformation was the most probable (m.p.) Newton diagram, the sum of total product recoil and D_e exceeded the available energy. This effect was most pronounced when the collision energy was nearest to threshold. While the most probable relative velocity of the collisions is given by the most probable Newton diagram, the steep rise of the total dissociation cross sections with increasing collision energy, displayed in Figs. 13 and 14, results in many more dissociations from the high energy side of the approximately symmetric fast atom incident energy distribution (remembering that $|\bar{V}| \approx |\bar{v}_{atom}|$) than from the lower energy side of the distribution. Thus the cross section weighted average collision energy ($\equiv E_{CM}'$) at which half of the observed dissociations occur at higher collision energies and half at lower collision energies will be larger than the most probable collision energy ($E_{CM}' > E_{CM}^{m.p.}$). This effect can be seen to be quite important when it is realized that even over the fairly narrow energy distributions characteristic of seeded heavy atom beams the total dissociation cross section at the high energy tail is frequently almost ten times larger than that at the low energy tail. Near the threshold, of course, the low energy tail cannot induce dissociation at all, so that the weighting of the higher collision energies in our dissociation observations becomes quite drastic. It seems clear that a correct averaging procedure must include the very strong dependence of $I_{CM}(u,\theta,V)$ on the relative velocity and that it would not be surpising if the (u,θ,V) dependences are all coupled.

The compromise which has been made in the analysis between the difficult and time-consuming full averaging procedure and the use of the most probable single Newton diagram involves sampling different center-of-mass points (corresponding to higher collision energies than that defined by the most probable Newton diagram) until a CM point is found which, serving as the origin of the CM system in a one Newton diagram LAB → CM transformation, leads to recoil velocity and energy peaks of the products which conserve both momentum and total energy. The in-plane center-of-mass differential cross section, $I_{CM}(u, \theta)$, shown in Fig. 12 for the Kr + CsBr system has been obtained using this weighted energy E^{w}_{CM} which best preserves both momentum and energy conservation. Similarly, all CM recoil peaks of the products of dissociative collisions for the systems listed in Table 1, and the subsequent energy transfer calculations, were obtained using the best E^{w}_{CM} in the LAB → CM transformation.

EXPERIMENTAL RESULTS AND DISCUSSION

A) Energy and Angular Distributions of Dissociation Products.

An example of the original laboratory distributions is shown in Fig. 4 for the near threshold dissociation of CsI by fast xenon. The smooth curves drawn through the energy distributions were transformed for each laboratory angle to plots of $P(E, \Theta)/v$. "Cartesian" contour maps, such as those shown in Figs. 5-9 for Cs^+ and Br^- produced in Xe(Kr) + CsBr collisions, were constructed from these plots. Figure 5 displays Cs^+ and Br^- contours resulting from a Xe + CsBr dissociation experiment with a most probable relative collision energy, $E^{m.p.}_{CM}$, of 6.00 eV. Examination of the Cs^+ contour map shows a large backward (with respect to the initial direction of the fast atom) peak symmetrically located on the relative velocity vector of the included most probable Newton diagram. It should be remembered that the ion scattering must be symmetric with respect to the relative velocity vector (although peaking on the relative velocity vector is, of course, not required), as, for any given impact parameter b, the spherical symmetry of the possible collision orientations results in all possible scattering planes being equally probable. The Cs^+ cartesian contour map of Fig. 5 also shows a small forward scattered peak located slightly off the relative velocity vector. The ratio of the peak intensity of the backward peak to that of the forward peak, remembering that multiplication by u^2 has not yet been taken into account, is about 18:1. Careful examination of the Br^- contour of Fig. 5 locates a large forward scattered peak and a small forward scattered shoulder close to the most probable center-of-mass point.

Figure 6 displays the Cs^+ cartesian contour map resulting from the dissociation of CsBr by fast xenon at a most probable relative collision energy of 6.84 eV. It is apparent from Fig. 6 that both the large backward and small forward peaks in the Cs^+ distribution have shifted sideways (toward a center-of-mass recoil angle of $\theta = 90°$) in comparison with the Cs^+ recoil distribution depicted in Fig. 5 ($E_{CM}^{m.p.} = 6.00$ eV). At $E_{CM}^{m.p.} = 6.84$ eV, the ratio of the peak intensity of the backward peak to that of the forward peak is approximately 13:1.

Figure 7 shows the Cs^+ cartesian contour map resulting from a Xe + CsBr experiment at a most probable collision energy of 9.46 eV.

Again it is seen that both the large backward peak and the small forward peak have shifted even more sideways, and the ratio of the peak intensities of the backward to forward peaks is about 6.5:1. It is clear that as the collision energy is increased the Cs^+ recoil peaks shift away from the relative velocity vector and the forward peak intensity, although consistently smaller than that of the backward peak, grows in size. These trends are maintained when the distributions are multiplied by u^2.

In Fig. 8, the Br^- cartesian contour map for a Xe + CsBr experiment with $E_{CM}^{m.p.} = 7.42$ eV is plotted. A large forward peak and a smaller but definite forward peak located close to the most probable center-of-mass are observed. Comparing this map with the Br^- distribution of Fig. 5, it is seen that an increase in collision energy does not appear to shift the angular location of the peaks, but the small forward peak located near the center-of-mass point clearly increases in intensity as the collision energy is increased.

Figure 9 displays Cs^+ and Br^- cartesian contour maps resulting from the dissociative collisions of Kr + CsBr at a most probable collision energy of 6.56 eV. Before multiplication by u^2, the Cs^+ distribution shows a large peak at the center-of-mass point and a very small shoulder in the forward direction slightly off the relative velocity vector. The Br^- contour map shows a single intense peak in the forward direction located well off the relative velocity vector.

In Fig. 10 the Rb^+ and I^- cartesian contour maps for a Xe + RbI experiment with $E_{CM}^{m.p.} = 5.97$ eV are plotted. The Rb^+ map shows two distinct forward scattered peaks. The less intense peak is located nearer the center-of-mass point and on the relative velocity vector while the more intense peak is a very broad peak, the peak angular position of which is also either near or on the relative velocity vector. This high recoil velocity peak provides a good example of the coupling between u and θ. Drawing a line through the $P(E, \theta)/v$ contour of highest intensity, 130, separability of the (u, θ) cross section dependence would require that this line describe a circle around the center-of-mass point, i.e., the separable function $U(u)$ should have only one value of u which maximizes it for all θ. At wide angles it is clear that the line bisecting this contour is closer to the center-of-mass point than at angles close to the relative velocity vector, and, therefore, the (u, θ) dependences of I_{CM} are not separable. The I^- contour has an intense backward peak off the relative velocity vector and a small peak, increasing in intensity as the collision energy increases (relative to another Xe + RbI experiment at $E_{CM}^{m.p.} = 4.94$ eV which is not shown), which appears in the forward direction near the relative velocity vector.

Figure 11 displays the cartesian contour maps of Cs^+ and I^- from dissociative collisions of Xe + CsI at $E_{CM}^{m.p.} = 5.97$ eV. The distributions of both ions show two distinct peaks and are quite similar. The ratio of the peak intensities of the large backward to smaller forward peak is larger for Cs^+, the heavier ion, than for I^-.

Finally, Fig. 12 presents an example of the CM differential cross sections of Cs^+ and Br^- from Kr + CsBr dissociative collisions obtained by multiplying the cartesian maps of Fig. 9 by u^2 using a Newton diagram characterized by E^w_{CM}.

The most important feature characteristic of the contour maps displayed in Figs. 5-12 is the existence of two distinct asymmetric peaks in the distribution of each ion at sufficiently high relative collision energies. A simple explanation for these two peaks is the existence of two distinct mechanisms which lead to dissociation. The relative dissociation efficiencies are reflected by the relative intensities within the two peaks. In the dissociation of CsBr by fast xenon, it is seen that the dominant dissociation mechanism produces Cs^+ peaking backward and Br^- peaking forward, while the less efficient mechanism produces Br^- slightly forward and Cs^+ farther forward. Similar observations are seen in the dissociation of RbI. The dominant dissociation mechanism in the Xe + RbI experiments results in backward scattered I^- and far forward scattered Rb^+, while the less efficient mechanism leads to forward scattered Rb^+ and farther forward I^-. These associations of ion recoil peaks are required if charge balance, conservation of momentum, and conservation of energy are to be preserved.

Since Rb^+ and Br^- are of approximately the same mass but opposite charge, as are Cs^+ and I^-, and since the cartesian contour maps for both sets of ions of approximately equal mass are very similar, it is apparent that the dissociation mechanisms and their resultant ion pair scattering are very strongly mass dependent. Further evidence of this mass dependence is found in the very similar nature of the cartesian contour maps of Cs^+ and I^- produced in the dissociation of CsI by xenon or krypton. In addition, for a given relative collision energy, comparison of the Cs^+ contour maps from the dissociation of CsI and CsBr (or the I^- contours from CsI and RbI) shows that the ratios of forward to backward peak intensities are very different, indicating that the mass dependence of each dissociation mechanism includes both atoms of the alkali halide.

In an attempt to characterize these two dissociation mechanisms, let us consider two limiting collision orientations - the rare gas atom hitting each side of the alkali halide in either a nearly collinear configuration or a nearly perpendicular configuration. The predictions of the differential scattering, predominantly determined in these systems by replusive forces, which each orientation provides will be compared. As will be discussed shortly with regard to the energy transfer computations listed in Table 1, conservation of momentum requires that in every case the rare gas atom recoils backward from its initial direction (0°) before collision. In the Xe + CsBr system, the principal dissociation mechanism results in Cs^+ and Xe scattered backward and Br^- scattered far forward from the center-of-mass of the three particles. In a nearly perpendicular collision, the only configuration which would result in Br^- scattering far forward would consist of xenon hitting the bromine atom directly with cesium approximating the role of a spectator. However, both the mass and velocity of xenon (based on three particle partitioning of the relative velocity vector) far exceed those of bromine, and such a two-body collision would almost surely result in xenon slowing down but continuing in its initial direction. This configuration would then result in Br^- and xenon scattered forward and Cs^+ scattered backward. In order to have xenon scattered backward, the impact parameter must be small. But for perpendicular collisions with small impact parameters, one does not expect to see two distinct peaks for each of the dissociated ions. Therefore, a collision configuration of xenon hitting CsBr nearly perpendicularly is not in agreement with experimental observations.

In a collinear collision there are two orientations of CsBr along the relative velocity vector providing different dissociation efficiencies, and it is easily seen that xenon is likely to scatter backward in collinear or near collinear collisions. If the collision is strictly collinear, the only configuration which could result in Br^- being scattered far forward requires xenon incident on the cesium atom, and qualitatively we would also expect xenon to recoil backward while Cs^+ remained fairly close the center-of-mass. From the point of view of the efficiency of impulsive momentum transfer that xenon incident on lighter bromine would transfer energy more efficiently to CsBr than xenon incident on cesium. But in a strictly collinear collision, which is a very rare event, the secondary collision between bromine and xenon is expected to transfer a large fraction of initial CsBr excitation back to the xenon atom. A more likely collision configuration for an efficient dissociation of CsBr is one in which xenon is incident on bromine in a near collinear configuration with a small but finite impact parameter. The impulsive collision between xenon and bromine then, not only causes the compression of the CsBr bond but also induces a rotational motion which sends Br^- into the forward and Cs^+ into the backward directions with respect to the direction of the initial xenon velocity. This is precisely what we found in our three dimensional classical trajectory calculations, to be mentioned later. The more efficient near collinear configuration is the one in which Xe or Kr is incident on the lighter atom of the alkali halide; this is expected to be a general phenomenon in all systems studied in this work.

There are some important qualitative observations which should be mentioned before we proceed with a more quantitative discussion. The striking similarity of the contour maps of Cs^+ and Br^- (Xe + CsBr, $E_{CM}^{m.p.} = 6.00$ eV, Fig. 5) to those of I^- and Rb^+ (Xe + RbI, $E_{CM}^{m.p.} = 5.97$ eV, Fig. 9) is quite interesting. The fact that the pairs Cs^+, I^- and Rb^+, Br^- have similar masses, different size and hardness, yet nearly identical contour maps, leads us to conclude that the mass ratio of the atoms in the colliding system plays a much more important role than the size and hardness of the atoms. The same conclusion could be derived from the similarity of the Cs^+ and I^- contour maps in the Xe + CsI experiment at $E_{CM}^{m.p.} = 5.97$ eV shown in Fig. 11.

Physically, we would expect that the efficiency of a particular dissociation mechanism would be directly related to the efficiency of the energy transfer to the relative motion of the atoms whose bond is to be broken. It is then of value to describe the relationship between the masses of the three interacting particles and the total transfer of initial collision energy to the relative motion of the diatomic, the relative ion pair recoil energy having been calculated from the center-of-mass differential dissociation cross sections. These center-of-mass differential dissociation cross sections have been obtained by multiplying the corresponding cartesian maps by u^2, where the $u = 0$ (CM point) was chosen to correspond to that Newton diagram, representing a relative collision energy E^{w}_{CM}, which best preserves energy conservation in the collision. It should be remembered that these in-plane distributions, when rotated 360° about the relative velocity vector, generate the differential dissociation cross sections in all space. From this cylindrical symmetry it can be seen that the total ion intensity summed over u for a given θ of the in-plane distribution must be weighted by multiplication of $\sin \theta$ in order to obtain the angular distribution of the total ion intensity as a function of θ summed over all ϕ. Thus, it is not unusual that the $I_{CM}(u, \theta)$ in-plane distribution will weight fairly intense contours which peak near the relative velocity vector (before multiplication by $\sin \theta$) so heavily that quite intense sideways peaks at lower laboratory velocities are left unobservable. This is perhaps the case in the Br^- differential dissociation cross section shown in Fig. 12. For these low intensity peaks resulting from the less preferred dissociation mechanism, overlap of intensity from the dominant peak has frequently made it difficult to accurately assign the peak position of the smaller peak.

Another difficulty in computation of the energy transfers arose in cases in which both ion peaks appeared off the relative velocity vector. It was necessary to determine whether these two peaks appear on the same or opposite sides of the relative velocity vector. In most cases it was possible to make this discrimination by requiring conservation of energy at some reasonable E_{CM}^{w}. This check of energy conservation was made by first finding the xenon (krypton) (u, θ) peak position using conservation of momentum and the two proposed ion peaks, and then summing the recoil energies in an attempt to achieve energy balance.

Having obtained the recoil peak positions of all three products, it has been possible to calculate the energy of recoil within the relative motion of the ion pair and thereby obtain a measure of the most probable energy transfer among those collisions which lead to dissociation. Table 1 summarizes the results of these calculations. This table lists for each set of collision partners the most probable collision energy $E_{CM}^{m.p.}$, the weighted collision energy E_{CM}^{w} which best leads to energy conservation, the peak position of the differential dissociation cross sections of the ion pairs on the (u, θ) surface, the recoil velocity peak position of the rare gas atom, the normalized relative energy of recoil between the alkali and halide ions (M^{+}, X^{-}) and two measures of the percentage of the initial relative collision energy which is transferrred to MX relative motion. If any dissociations are to occur when $E_{CM} = D_e - E_{int} = D'$, i.e. when the relative kinetic energy just equals the average effective dissociation threshold, namely the difference between the dissociation energy and the internal energy, the separated products would possess no energy of recoil, the energy transfer efficiency $[D' + E_{M^{+}, X^{-}} (=0)]/E_{CM}$ would have to be 100%, and the cross section for dissociation would be approximately zero. As the collision energy is increased, the energy transfer efficiency would not have to be 100%, and energy conservation would no longer restrict the M^+, X^- relative recoil energy to zero. The total amount of energy transferred to the relative motion of the diatomic, then, is equal to the effective dissociation energy D' plus the M^+, X^- relative recoil energy. The quantity $\{[D' + E_{M^+,X^-}]/E^w_{CM}\}$ x 100% thus represents the most probable percentage energy transfer among those collisions which lead to dissociation. Because the true peak in the energy transfer distribution for these atom-diatomic molecule collisions may at some collision energies and orientations be too low to produce dissociation while the high energy transfer tail of the distribution could result in dissociation with small E_{M^+, X^-}, the percentage energy transfer calculated from the above expression will not be very meaningful as a measure of the most probable energy transfer in these weakly dissociative cases. In order to obtain a general feeling about the trend in energy transfer for a given collision orientation as a function of collision energy at energies so low that E_{M^+, X^-} is very small, the quantity $\{E_{M^+, X^-}/[E^w_{CM} - D]\}$ x 100% has been tabulated. This expression calculates the percentage of excess total energy over and above that needed to induce dissociation which is transferred to the relative motion of M^+ and X^-. For those experiments, indicated by asterisks in Table 1, in which E_{M^+, X^-} is small and the most probable energy transfer in the collision does not induce dissociation, this latter quantity gives a good indication of how energy transfer is changing as a function of relative collision energy. For all cases without an asterisk, E_{M^+, X^-} is large enough so that the quantity $\{[D' + E_{M^+, X^-}]/E^W_{CM}\}$ should provide a good measure of the most probable energy transfer.

Because of the internal consistency of the differential dissociation cross sections summarized in Table 1 and the relative total dissociation cross sections which we have measured, it is of value to present these latter results at this time. The total relative cross sections for the dissociation of CsI, CsBr, RbI, and KI upon impact with xenon and krypton have been obtained as functions of the center-of-mass relative kinetic energy. The results are shown in Fig. 13 for xenon and Fig. 14 for krypton.

One very obvious feature of these measurements is the extremely strong similarity of the CsBr and RbI results. The total relative dissociation cross sections of CsBr and RbI are virtually indistinguishable in collisions with xenon and also with krypton. While we might expect, and indeed do observe, less asymmetry in peak heights resulting from hitting on the rubidium (85.47 a.m.u.) versus iodine (126.91 a.m.u.) ends, than in the peak heights resulting from hitting on the bromine (79.91 a.m.u) versus cesium (132.91 a.m.u.) ends, the total masses of CsBr and RbI are 212.83 a.m.u. and 212.38 a.m.u., respectively, and since the total dissociation cross section sums the dissociation probabilities for each orientation, it is apparent that the small mass differences between cesium and iodine and between bromine and rubidium compensate for each other. Table 1 reflects the differences in peak height asymmetries in energy transfer terms. For the preferred dissociation mechanism, labeled (A) in Table 1, Xe → BrCs ($E_{CM}^{m.p.}$ = 6.00 eV) results in a very large 95.3% of the initial energy transferred to the relative motion of CsBr. For the less asymmetric (in both mass and peak height ratios) RbI case, the preferred Xe → RbI ($E_{CM}^{m.p.}$ = 5.97 eV) orientation leads to a slightly smaller 92.9% energy transfer. For the less preferred Xe → IRb orientation, it is seen that the relative ion recoil energy is only 0.015 eV. The peak angles in θ for all three products are within 10° of the relative velocity vector. It seems clear that the most probable energy transfer for xenon hitting iodine in RbI almost collinearly at this energy will not induce dissociation and, therefore, only the high energy transfer tail contributes to the dissociation. This can be seen by comparing the total energy transfer of 70% with the percentage of excess energy which is transferred, less than 1%. We could expect similar results for Xe → CsBr collisions, but the very small intensities of these peaks make it difficult to confidently assign peak positions.

Actually, the qualitative features of the efficiency of energy transfer discussed above and the energy dependence of the total dissociation cross sections shown in Figs. 13 and 14 can be easily understood from a simple consideration of a hard sphere collision between an atom and a diatomic molecule. This understanding requires the assumption (verified, as discussed later, by classical trajectory calculations) that the forward scattered ion corresponds to that atom impulsively struck in a near collinear collision by the incident rare gas atom.

Let us consider the following collision configuration:

where Ⓐ–Ⓑ represents the alkali halide and Ⓒ the incoming fast atom. If A, B, and C are hard spheres and the initial AB internal energy is zero, it can easily be shown through energy and momentum conservation that the fraction (E_{AB}/T) of the initial relative kinetic energy (T) which is transferred to energy of relative motion of AB (E_{AB}) following a single B-C collision depends only on the masses of the three particles involved, and is given by[32]

$$\frac{E_{AB}}{T} = \frac{4m_Am_Bm_C(m_A + m_B + m_C)}{(m_A + m_B)^2(m_B + m_C)^2} \qquad (4),$$

where m_A, m_B, and m_C are the masses of the colliding atoms. It can be seen that the denominator of equation (4) is asymmetric in m_A and m_B, and consequently, for $m_A \neq m_B$, we would expect different fractional energy transfers when the two different atoms of the diatomic serve as the central atom B. Thus for the orientations Xe → BrCs and Xe → CsBr we find respectively that $E^{Br}/T = 95\%$ and $E^{Cs}/T = 61\%$; these calculated hard-sphere fractional energy transfers may be compared with the experimental values of $E^{Br}_{exp}/T = 95.3\%$ and $E^{Cs}_{exp}/T = 74\%$. Here 74% represents the minimum percentage energy transfer necessary to induce dissociation under the experimental conditions ($E^{m.p.}_{CM} = 6.00$ eV) depicted in Fig. 5, and E^{Br} and E^{Cs} represent the energy of relative motion between Cs and Br when Br and Cs act as the center atoms.

The fractional energy transfers calculated for various colliding species with different configurations by a hard sphere impulsive collision model are tabulated in Table II. A comparison of these calculated values with the experimental values, $\left[(E_{M^+,\ X^-} + D)/E_{CM}^{W}\right] \times 100\%$, listed in Table I indeed demonstrates very good agreement. For example, when comparing the more preferred (light-atom) orientation, labelled (A) in Table I, with the less preferred (heavy-atom) orientation (B), it is seen that the size of the energy transfer is reflected in the differential cross section peak heights. For the strongly asymmetric Xe + RbI system, Xe → RbI transfers $E_{exp}^{Rb}/T = 92.9\%$ (calculated hard-sphere $E^{Rb}/T = 92.4\%$), while Xe → IRb (calculated $E^{I}/T = 65.1\%$, $E^{I} \approx 3.9$ eV $< D'$ for $E_{CM}^{m.p.} = 5.97$ eV) only rarely leads to dissociation. For the Xe + CsI experiment at $E_{CM}^{m.p.} = 7.37$ eV, E_{exp}^{I} (Xe → ICs) and E_{exp}^{Cs} (Xe → CsI) are 1.76 eV and 1.18 eV respectively. These are very substantial recoil energies, and in this case it is thus reasonable to say that the most probable transfer in near collinear collisions does lead to dissociation. By way of comparison, $E_{exp}^{I}/T = 80.5\%$ and $E_{exp}^{Cs}/T = 72.6\%$, while the calculated equivalents are $E^{I}/T = 77\%$ and $E^{Cs}/T = 73.5\%$.

Also obvious from Table I are the additional model-corroborating observations that xenon transfers energy more efficiently than krypton and that, for the same initial relative kinetic energies, Xe → RbI transfers energy more efficiently than Xe → CsI. Finally, it can be seen from the three Xe + CsI experiments at different energies that the most probable percentage energy transfer increases with energy, as demonstrated by the increase in the percentage of excess initial energy transferred to the relative energy of ion separation.

B) Collision Energy Dependence of Total Dissociation Cross Sections.

Figure 13 shows that at low energies only slightly above threshold the total cross section for xenon-induced dissociation of CsI is lower than that of the other three salts studied. This is not surprising in view of the fact that E_{AB}/T is about 75% for both orientations, Xe → ICs and Xe → CsI. This is much lower than the 97% and ~94% transfer efficiencies obtainable for Xe → KI and Xe → RbI (BrCs). Thus, at low collision energies the preferred light-atom orientations, Xe → KI (BrCs, RbI), efficiently transfer sufficient energy to induce dissociation while neither orientation in CsI effectively promotes dissociation. When the collision energy is raised above 6.5 eV, however, the CsI dissociation cross section becomes larger and has a steeper slope than that of CsBr, RbI and KI. This result can be easily understood since both orientations of CsI with E/T of ~75% dissociate increasingly efficiently at higher energies while the configurations Xe → IK, Xe → CsBr, and Xe → IRb, with respective E_{AB}/T values of 42%, 61% and 65%, contribute to the dissociation with only part of their energy transfer distributions. At higher energies between 6.5-10 eV, then, the observed trend, $\sigma(\mathrm{CsI}) > \sigma(\mathrm{CsBr}) = \sigma(\mathrm{RbI}) > \sigma(\mathrm{KI})$, is expected from our model.

From Fig. 14 it is seen that at low energies the total relative krypton-induced dissociation cross sections follow the trend $\sigma(\mathrm{KI}) > \sigma(\mathrm{RbI}) = \sigma(\mathrm{CsBr}) > \sigma(\mathrm{CsI})$. In addition, it is observed that the threshold extrapolated from the Kr + CsI curve is larger than the theoretical threshold energy of 4.37 eV for producing Cs^+ and I^-, and that at energies between 6.5 - 8 eV the CsI slope becomes steeper than the slopes for the other salts. These results are quite similar in nature to those observed in the low energy regime of Xe-alkali halide (MX) dissociations. In Kr-MX collisions the mass effects are much more pronounced than in the corresponding Xe-MX encounters. This is to be expected, since the E_{AB}/T values for Kr → KI, Kr → RbI (BrCs), and Kr → ICs are 100%, 85%, and 65% respectively. The significant differences in the dissociation cross sections for these systems at low energies are thus due to the large differences in the efficiencies of energy transfer. Apparently, with an average E_{AB}/T of 63%, Kr + CsI does not dissociate efficiently even at a collision energy of 8 eV.

It is of interest to examine the metal halide dissociation studies of Parks et al.[10-15] in the light of the dynamical picture which has emerged from the present work. Parks et al. have performed experiments to determine the absolute total cross sections for dissociation of TlF, TlCl, TlBr, TlI, CsCl and the corresponding dimers to ion pairs upon impact with hyperthermal xenon and krypton from a seeded supersonic molecular beam source. Their results for xenon-induced dissociation show that $\sigma(\mathrm{TlCl}) \approx 1/3\sigma(\mathrm{CsCl}) \approx 10\sigma(\mathrm{TlF}) \approx 10\sigma(\mathrm{TlBr}) \approx 1000\sigma(\mathrm{TlI})$. Their krypton-induced dissociation cross sections are of similar magnitudes except for TlBr where $\sigma^{Xe}(\mathrm{TlBr}) \approx 10\sigma^{Kr}(\mathrm{TlBr})$. One major difference between alkali halide and thallium halide ionic dissociation cross sections is immediately apparent: in the present work, at a given

E_{CM} collision energy, the total cross sections for dissociation to ion pairs observed among all the alkali halide/rare gas combinations sampled ranged within a factor of two of one another; dissociative ion pair formation from the thallium halides, on the other hand, varied over one to three orders of magnitude in cross section. The mass trends and dynamical phenomena demonstrated in the present studies should be directly applicable to the collision-induced dissociation of thallium halides. The principal (and, because of the large mass of the thallium atom, perhaps only) active dissociation mechanism likely consists of the rare gas atom incident on the halide atom in a near collinear configuration; forward peaking of the halide ion and backward peaking of the thallium ion and recoiling rare gas atom may also be expected. Yet it appears unlikely that the energy transfer efficiencies which so dominate ion pair formation in alkali halide dissociation can by themselves explain the large variations in dissociative ion pair formation cross sections observed for the thallium halides. This can be seen by noting that although the impulsive model predicts for the configurations Xe → FTl, Xe → ClTl, Xe → BrTl and Xe → ITl percentage energy transfers (E_{AB}/T, see equation (4)) of 64.2%, 88.3%, 98.9% and 86.1% respectively, the dissociative ion pair formation cross sections follow the trend $10\sigma(\mathrm{TlF}) \approx \sigma(\mathrm{TlCl}) \approx 10\sigma(\mathrm{TlBr}) \approx 1000\sigma(\mathrm{TlI})$.

Parks et al. postulate that the apparent lack of ion pair formation in TlBr and TlI dissociation is due to the dominance of the adiabatic dissociation channel to separated neutral atoms while they attribute the low yield from TlF to inefficient collisional energy transfer.

Using tabulated bond energies, molecular constants and thermodynamic data, they have constructed two-body potential energy curves such that the splitting of the two lowest (identical symmetry) states in the avoided crossing region reproduces the ion/neutral branching ratios they have estimated from their data. Since they have not made measurements to characterize the neutral exit channel dissociation products, such estimates require the as yet unproven assumption that the total dissociation cross sections (ion plus neutral pairs) are comparable for TlCl, TlBr and TlI. Clearly the magnitudes of these summed dissociation cross sections will be strongly dependent on energy transfer efficiency considerations analogous to those found in the present studies.

C) Classical Trajectory Calculations.

In an effort to qualitatively understand the rich dynamical features experimentally observed in the present work, limited three-dimensional classical trajectory calculations were performed on the Xe + CsBr system colliding with an energy E_{CM}^{W} = 6.23 eV. (Note that this collision energy corresponds to that sampled in the experiment plotted in Fig. 5.) The primary objective of these calculations was the generation of a pictorial description of the nature of those collision trajectories which most frequently result in dissociative ion pair formation. No attempt was made to utilize the approximately transformed experimental data to iteratively define the most appropriate potential energy representation of the colliding system.

Throughout all of the calculations a Rittner potential[33] was used to represent the Cs^+-Br^- interaction and exponential replusion + R^{-4}, R^{-6} attraction potentials[34] were used to model the Xe-Cs^+ and Xe-Br^-

interactions. Explicity we have

$$V_{CsBr}(r) = A\exp(-\frac{r}{\rho}) - \frac{e^2}{r} - \frac{e^2(\alpha_{Cs^+} + \alpha_{Br^-})}{2r^4} - \frac{C}{r^6} - \frac{2e^2\alpha_{Cs^+}\alpha_{Br^-}}{r^7}$$

and

$$V_{BC}(R) = Q\exp(-\frac{R}{\sigma}) - \frac{e^2\alpha_C}{2R^4} - \frac{3\alpha_C^2 I_C}{4f_C R^6} - \frac{3I_B I_C \alpha_B \alpha_C}{2(I_B+I_C)R^6} ,$$

where BC may represent either Cs^+Xe or Br^-Xe. The numerical values used for the parameters in the above expressions are as follows: polarizabilities α_{Br^-}, α_{Cs^+}, α_{Xe} = 4.5 $Å^3$, 2.5 $Å^3$, 4.01 $Å^3$ respectively;[35] repulsion, van der Waals constants A, ρ, C = 4690 eV, 0.361 Å, 135 eV $Å^6$ respectively;[35] ionization potentials I_{Br^-}, I_{Cs°, I_{Xe} = 3.5 eV, 3.9 eV, 12.1 eV respectively;[34] oscillator strength f_{Xe} = 5.6 (dimensionless);[34] repulsion constants Q_{Cs^+Xe}, σ_{Cs^+Xe} = 3230 eV, 0.363 Å respectively;[36] replusion constants Q_{Br^-Xe}, σ_{Br^-Xe} = 1952 eV, 0.465 Å respectively.[36] The three applicable two-body potential energy curves are plotted as functions of internuclear distance in Fig. 15.

Three different series of trajectory calculations were carried out. First, dissociated ion contour maps averaged over randomized initial conditions were generated as functions of internal angular momentum quantum number and total internal energy. These maps demonstratively reproduce the principal features of the experimentally measured contours, e.g., Cs^+ peaking backward and Br^- peaking forward, and show only minor variations over the range of internal molecular parameters representative of the experimental conditions. Second, calculations at fixed impact parameter and randomized collision orientation in a coplanar configuration were performed to identify and to group sequences of dissociative trajectories. Finally, individual trajectories were traced ($\vec{Q}_A$, $\vec{Q}_B$, $\vec{Q}_C$, $\vec{V}_A$, $\vec{V}_B$, $\vec{V}_C$, R_{AB}, R_{BC}, R_{AC}, V'_{AB}, V'_{BC}, V'_{AC} versus time) and the dominant features of the dissociation mechanism were cataloged. Generally speaking, compressive collisions of the incoming xenon atom with the bromine (light atom) end of the alkali halide in near collinear configurations most frequently result in dissociative ion pair formation. Table III lists for fixed impact parameters of 1 Å and 2 Å the approximate percentage of dissociative trajectories initiated by Xe → Br, Cs compressions/expansions and the resultant percentages for product scattering into the backward versus forward hemispheres. Observations which are immediately apparent from Table III are the dominance of the xenon on bromine collision configuration and the qualitative similarity of the calculated recoil product peak height asymmetries with those measured in experiment. It is interesting and not particularly surprising to note that the inefficient energy transfer xenon on cesium collision configuration contributes a smaller fraction to the dissociation at the more 'grazing' impact parameter of 2 Å than it does at b = 1 Å.

Two typical dissociative trajectories are traced in Figs. 16 and 17. The collision event depicted in Fig. 16 is representative of the dominant dissociation mechanism observed throughout this work. Xenon is incident with small impact parameter on bromine in a near collinear collision; Br^- is seen to peak forward while Cs^+ and Xe recoil backward. Figure 17 demonstrates the collidant pathways for the less preferred dissociation mechanism, xenon incident on cesium atom in a near collinear configuration. In this particular case Cs^+ scatters forward, Br^- recoils to the side and Xe scatters backward.

SUMMARY

At energies just a few electron volts above threshold the differential dissociation cross sections for ion pair formation contain two peaks corresponding to two limiting case dissociation mechanisms. As the collision energy is increased, these diffuse peaks are seen to shift sideways off the relative velocity vector and to become more balanced in intensity reflecting both the increased importance or larger impact parameter collisions (bdb weighting) and the enhancement in dissociation probability for collision configuration in which the energy transfer efficiency is less than ideal. Mass and orientation effects observed in both the experiments and the trajectory calculations are consistent in their definition of these limiting case dissociation mechanisms-near collinear collisions of the rare gas atom with the light (most efficient) and heavy (less preferred) ends of the alkali halide molecule.

ACKNOWLEDGEMENTS

This work was supported by the U.S. Atomic Energy Commission and Louis Block Funds of the University of Chicago while the authors were associated with the University of Chicago. We are grateful to

Dr. James Muckerman for providing the programs for classical trajectory calculations and to Dr. William Lester for assistance in carrying out trajectory calculations at IBM Research Laboratory, San Jose. The final stage of this work was supported by the Division of Chemical Sciences, Office of Basic Energy Sciences, U. S. Department of Energy under contract No. W-7405-Eng-48. H.H. thanks the Deutsche Forschungsgemeinschaft for support.

REFERENCES

a) Present address: Applied Physics Division, Sandia Laboratories, Livermore, California 94550.

b) Present address: Department of Physics, Cornell University, Ithaca, New York 14853.

c) Present address: Fakultät fur Physik der Universität Freiburg, Freiburg im Breisgau, Germany.

d) Present address for Y. T. Lee.

1. R.S. Berry, T. Cernoch, M. Coplan and J.J. Ewing, J. Chem. Phys. 49. 127 (1968).
2. J.J. Ewing, R. Milstein and R.S. Berry, J. Chem. Phys. 54, 1752 (1971).
3. R. Milstein, Ph.D. Thesis, The University of Chicago, Chicago, Illinois, 1973.
4. A. Mandl, E.W. Evans and B. Kivel, Chem. Phys. Lett. 5, 307 (1970); A. Mandl, B. Kivel and E.W. Evans, J. Chem. Phys. 53, 2363 (1970).
5. A. Mandl, J. Chem. Phys. 55, 1918 (1971).
6. A. Mandl, J. Chem. Phys. 55, 2922 (1971).
7. V.H. Hartig, H.A. Olachewski, J. Troe and H.G. Wagner, Ber. Bunsenges. Physik. Chem. 72, 1016 (1968).
8. K. Luther, J. Troe and H.G. Wagner, Ber. Bunsenges. Physik. Chem. 76, 53 (1972).
9. F.P. Tully, Y.T. Lee and R.S. Berry, Chem. Phys. Lett. 9, 80 (1971).
10. E.K. Parks and S. Wexler, Chem. Phys. Lett. 10, 245 (1971).

11. E.K. Parks, N.J. Hansen and S. Wexler, J. Chem. Phys. 58, 5489 (1973).

12. E.K. Parks, A. Wagner and S. Wexler, J. Chem. Phys. 58, 5502 (1973).

13. E.K. Parks, J.G. Kuhry and S. Wexler, J. Chem. Phys. 67, 3014 (1977).

14. S.H. Sheen, G. Dimoplon, E.K. Parks and S. Wexler, J. Chem. Phys. 68, 4950 (1978).

15. E.K. Parks, S.H. Sheen and S. Wexler, J. Chem. Phys. 69, 1190 (1978).

16. R.D. Levine, Chem. Phys. Lett. 11, 109 (1971).

17. R.D. Levine and B.R. Johnson, Chem. Phys. Lett. 7, 404 (1970).

18. R.D. Levine and B.R. Johnson, Chem. Phys. Lett. 8, 501 (1971).

19. R.D. Levine and R.B. Bernstein, Chem. Phys. Lett. 11, 552 (1971).

20. H. Fan, J. Chem. Phys. 55, 4628 (1971).

21. L.G. Piper, L. Hellemans, J. Sloan and J. Ross, J. Chem. Phys. 57, 4742 (1972).

22. This terminal velocity is characteristic of seeded beam expansions in carrier gases of specific heat 5/3. For hydrogen as the carrier gas, expansion yields lower terminal velocities than those predicted for diatomic carrier gases ($C_p/C_v = 7/5$), an observation attributed to hydrogen's very slow rotational relaxation.

23. U. Buck, H. Pauly, D. Pust and J. Schleusner, 9th International Symposium on Rarefied Gas Dynamics p.C. 10-1, Göttingen 1974 (eds. M. Becker, M. Fiebig) DFVLR-Press, Porz-Wahn, Germany

24. E.A. Entemann, Ph.D. Thesis, Harvard University, Cambridge, Massachusetts, 1967.

25. P.E. Siska, Ph.D. Thesis, Harvard University, Cambridge, Massachusetts, 1970.

26. The averaging effect of beam divergence has not been included since trial calculations have shown that this effect is negligible compared with that of velocity-averaging. See Ref. 25.

27. J.M. Farrar, J.M. Parson and Y.T. Lee, 4th International Conference on Molecular Beams (1973), Abstract.

28. S.J. Riley and D.R. Herschbach, K + CCl_4 system, unpublished results.

29. N. Abuaf, Ph.D. Thesis, Princeton University, Princeton, New Jersey, 1966.

30. H. Haberland, F.P. Tully and Y.T. Lee, 8th International Symposium on Rarefied Gas Dynamics, p. 533 (Stanford, 1972).

31. F.P. Tully, Ph.D. Thesis, The University of Chicago, Chicago, Illinois, 1973.

32. B.H. Mahan, J. Chem. Phys. 52, 5221 (1970).

33. E.S. Rittner, J. Chem. Phys. 19, 1030 (1951).

34. M.G. Menendez, M.J. Redmon and J.F. Aebischer, Phys. Rev. 180, 69 (1969).

35. C. Maltz, Chem. Phys. Lett. 3, 707 (1969).

36. K. Spears, J. Chem. Phys. 57, 1842 (1972).

TABLE 1

MOST PROBABLE ENERGY TRANSFER TO THE RELATIVE MOTION OF THE DISSOCIATED ION PAIR CALCULATED FROM THE PEAKS OF THE DIFFERENTIAL DISSOCIATION CROSS SECTIONS

Colliding Species		(eV) $E_{CM}^{m.p.}$	(eV) E_{CM}^{W}	(u, θ) peak positions in (x 10^4 cm/sec, degrees)			(eV) E_{M^+, X^-}	$\frac{E_{M^+, X^-} + D'}{E_{CM}^{W}}$ X 100%	$\frac{E_{M^+, X^-}}{E_{xs}}$ X 100%
				+ ion	- ion	Rare Gas Atom			
Xe + CsBr	(A)	6.00	6.23	(6.2, 180°);	(18.35, 0°);	(4.89, 180°)	1.46	95.3	83.4
Kr + CsBr	(A)	6.56	6.73	(6.41, 106°);	(15.3, 22.5°);	(18.7, -125°)	0.48	73.6	21.0
Xe + RbI	(A)	5.97	6.04	(16.5, 5°);	(5.32, 155°);	(6.81, -153°)	1.389	92.9	89.3
	(B)	5.97	6.04	(7.6, 10°);	(10.55, 5°);	(15.1, -173°)	0.015	70.2*	0.83
Xe + CsI	(A)	4.58	5.06	(3.9, 39°);	(7.8, -39°);	(9.21, 166°)	0.153	85.4*	17.2
Xe + CsI	(A)	5.97	6.43	(6.79, 82°);	(12.65, -14.5°);	(13.33, -164°)	0.588	74.0	26.0
Xe + CsI	(A)	7.37	7.44	(8, 150°);	(18.65, 0°):	(11.73, -160°)	1.76	80.5	55.0
	(B)	7.37	7.44	(16.75, 0°)	(7.0, 115°);	(15.37, -156°)	1.18	72.6	36.9
Kr + CsI	(A)	6.77	7.44	(7.55, 95°)	(14.0, -13°);	(20.84, -160°)	0.86	67.7	26.4
	(B)	6.77	7.44	(12.21, 0°);	(7.43, 88°);	(22.73, -150°)	0.526	63.1	16.1

(A) Refers to calculations for the dominant dissociation mechanism.

(B) Refers to calculations based on the less preferred dissociation mechanism.

Table II. Hard Sphere Impulsive Collision Model for Collisional Energy Transfer, E/T*

Systems	E/T* (%)	Systems	E/T* (%)
Xe → CsI	73.5	Kr → CsI	61.3
Xe → ICs	77.1	Kr → ICs	64.8
Xe → RbI	92.4	Kr → RbI	83.3
Xe → IRb	65.1	Kr → IRb	53.8
Xe → CsBr	60.7	Kr → CsBr	49.6
Xe → BrCs	95.0	Kr → BrCs	87.1
Xe → KI	96.8	Kr → KI	99.8
Xe → IK	42.2	Kr → IK	34.0

*Fractional energy transfers, E/T are calculated from equation (4).

Table III. Semi-Quantitative* Grouping of Co-Planar Dissociative Collision Trajectories.

	Nature of First Collision, % of Events				
	$\mathrm{Xe}\rightarrow\mathrm{Br}(\mathrm{C})^{a}$	$\mathrm{Xe}\rightarrow\mathrm{Br}(\mathrm{E})^{b}$	$\mathrm{Xe}\begin{matrix}\nearrow\mathrm{Br}\\ \searrow\mathrm{Cs}\end{matrix}(\mathrm{E})$	$\mathrm{Xe}\rightarrow\mathrm{Cs}(\mathrm{C})$	$\mathrm{Xe}\rightarrow\mathrm{Cs}(\mathrm{E})$
b = 1 Å	59	8	19	12	2
b = 2 Å	41	30	26	3	1

		Angular Distribution of Products		
		Br^{-}	Cs^{+}	Xe
b = 1 Å	Backward	16	72	91
	Forward	84	28	9
b = 2 Å	Backward	4	92	49
	Forward	96	8	51

Initial Conditions: Rotational quantum number = 400
Internal Energy $(E_{vib} + E_{rot}) = 0.12 \times 10^{-11}$ erg
Relative Collision Energy $= 0.998 \times 10^{-11}$ erg

*Based on 70 dissociative trajectories for each impact parameter.

[a] (C) = alkali halide bond compression.

[b] (E) = alkali halide bond expansion.

FIGURE CAPTIONS

Fig. 1. Schematic drawing of the experimental arrangement.

Fig. 2. Typical energy spectra of xenon and krypton beams produced upon ionization by electron bombardment followed by retarding field analysis of the resultant ions. Singly, doubly and triply ionized xenon and singly and doubly ionized krypton are produced upon bombardment with 140 eV electrons. The pulse height threshold discriminator was adjusted to favor the detection of multiply charged ions.

Fig. 3. Relationship between laboratory and center of mass coordinate systems.

Fig. 4. An example of the laboratory energy distributions of a dissociated pair as plotted by an X-Y recorder. These distributions of Cs^+ and I^- result from near threshold dissociative collisions of xenon and cesium iodide.

Fig. 5. Cartesian contour maps of Cs^+ and Br^- resulting from dissociative Xe + CsBr collisions at a most probable relative collision energy of 6.00 eV.

Fig. 6. Cartesian contour map of Cs^+ resulting from dissociative Xe + CsBr collisions at a most probable relative collision energy of 6.84 eV.

Fig. 7. Cartesian contour map of Cs^+ resulting from dissociative Xe + CsBr collisions at a most probable relative collision energy of 9.46 eV.

Fig. 8. Cartesian contour map of Br^- resulting from dissociative Xe + CsBr collisions at a most probable relative collision energy of 7.42 eV.

Fig. 9. Cartesian contour maps of Cs^+ and Br^- resulting from dissociative Kr + CsBr collisons at a most probable relative collision energy of 6.56 eV.

Fig. 10. Cartesian contour maps of Rb^+ and I^- resulting from dissociative Xe + RbI collisions at a most probable relative collision energy of 5.97 eV.

Fig. 11. Cartesian contour maps of Cs^+ and I^- resulting from dissociative Xe + CsI collisions at a most probable relative collision energy of 5.97 eV.

Fig. 12. Center of mass differential dissociation cross sections of Cs^+ and Br^- calculated using a one Newton diagram LAB→CM transformation of the Cartesian contour map displayed in Fig. 9. The dissociated ions resulted from Kr + CsBr collisions at a most probable relative collision energy of 6.56 eV. The best weighted collision energy used in the coordinate transformation is 6.73 eV.

Fig. 13. Relative total cross sections for the dissociation of CsI, CsBr, RbI and KI to ion pairs upon impact with fast xenon as a function of relative collision energy.

Fig. 14. Relative total cross sections for the dissociation of CsI, CsBr, RbI and KI to ion pairs upon impact with fast krypton as a function of relative collision energy.

Fig. 15. Two-body potential energy curves used to model the Xe + CsBr interaction in 3-D classical trajectory calculations.

Fig. 16. A representative trajectory map for the Xe→BrCs collision configuration. The numerical indices refer to specific time steps during the collision event, b = 1 Å.

Fig. 17. A representative trajectory map for the Xe→CsBr collision configuration. The numerical indices refer to specific time steps during the collision event, b = 0.

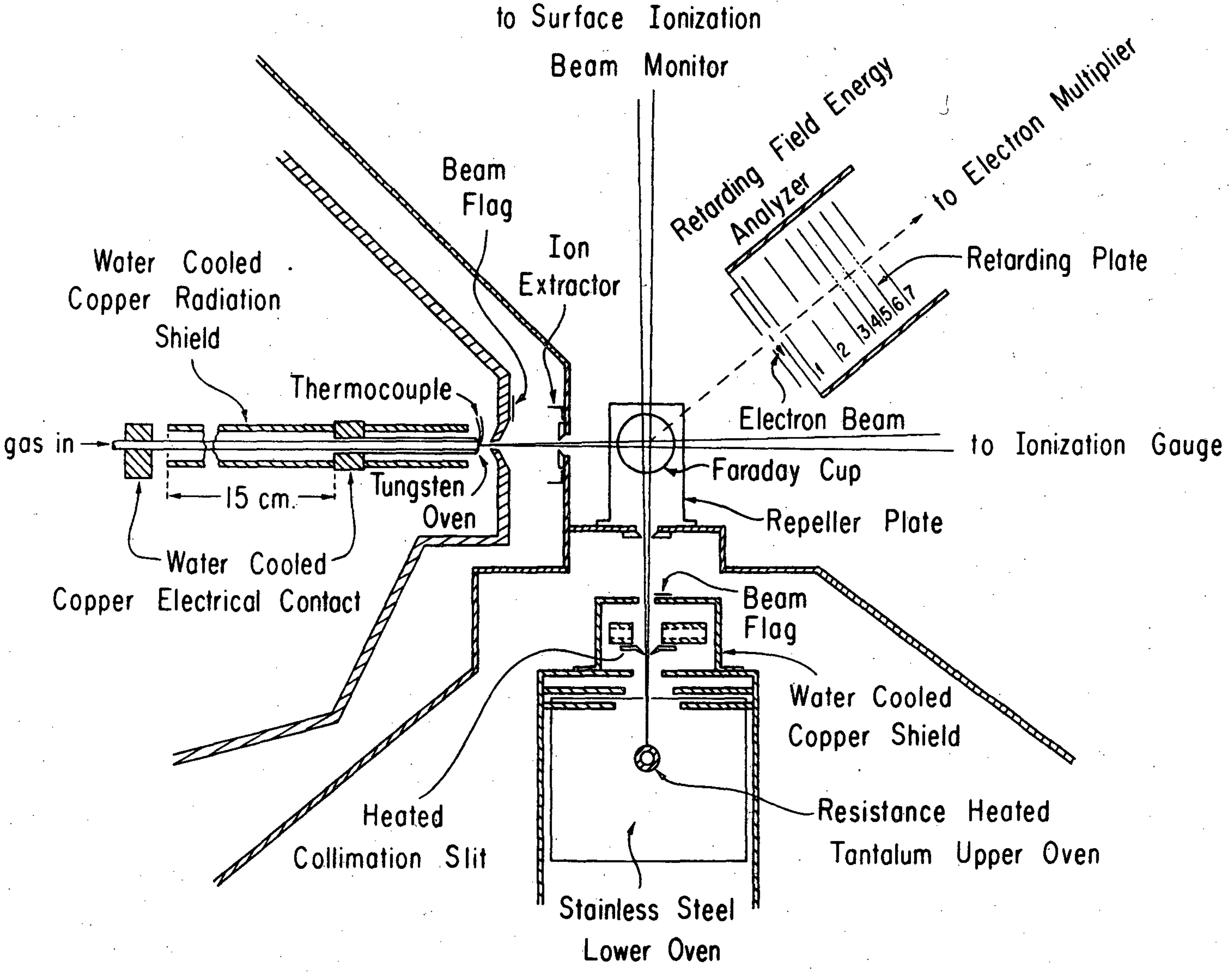

XBL 802-7974

Fig. 1

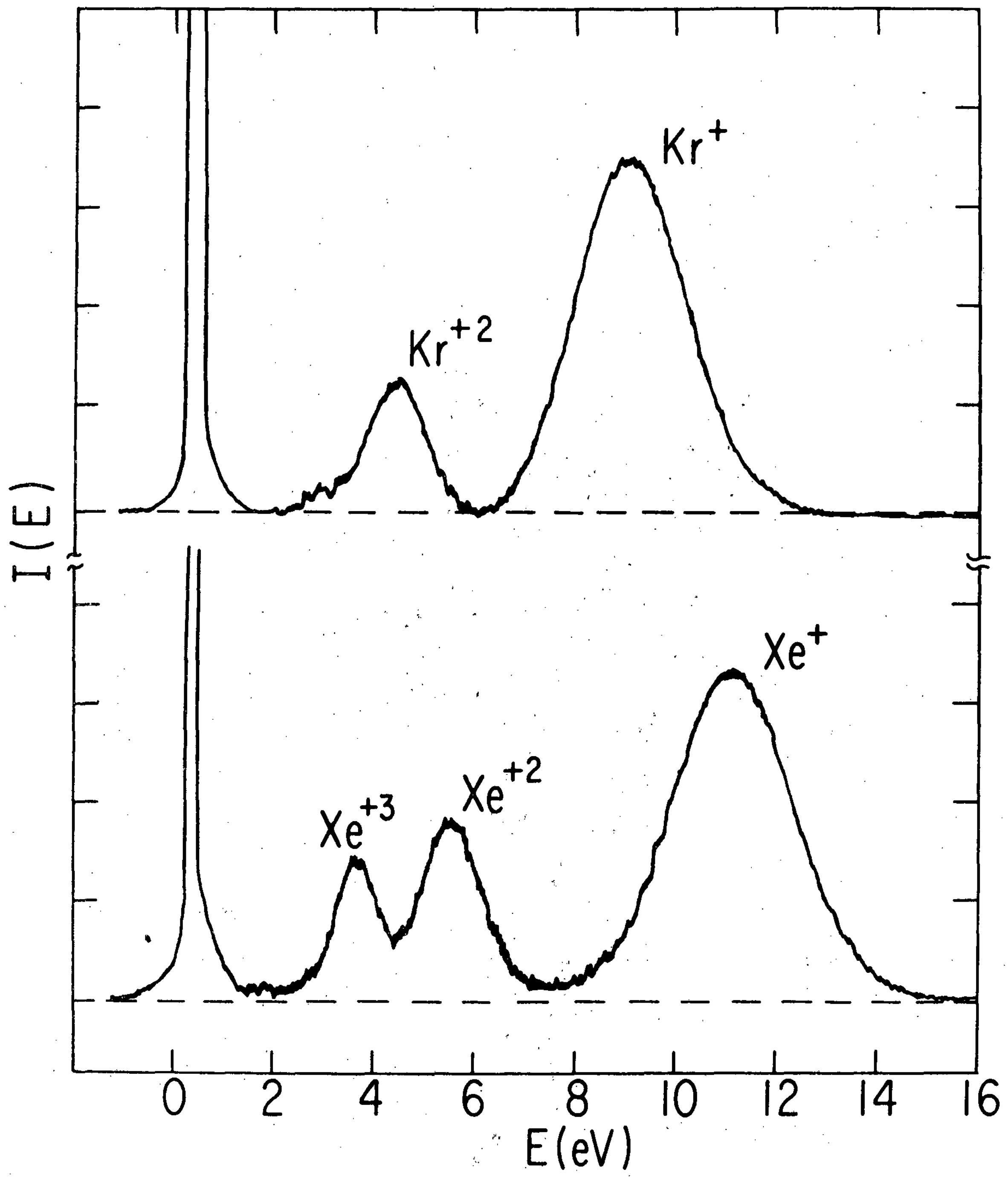

XBL 802-7975

Fig. 2

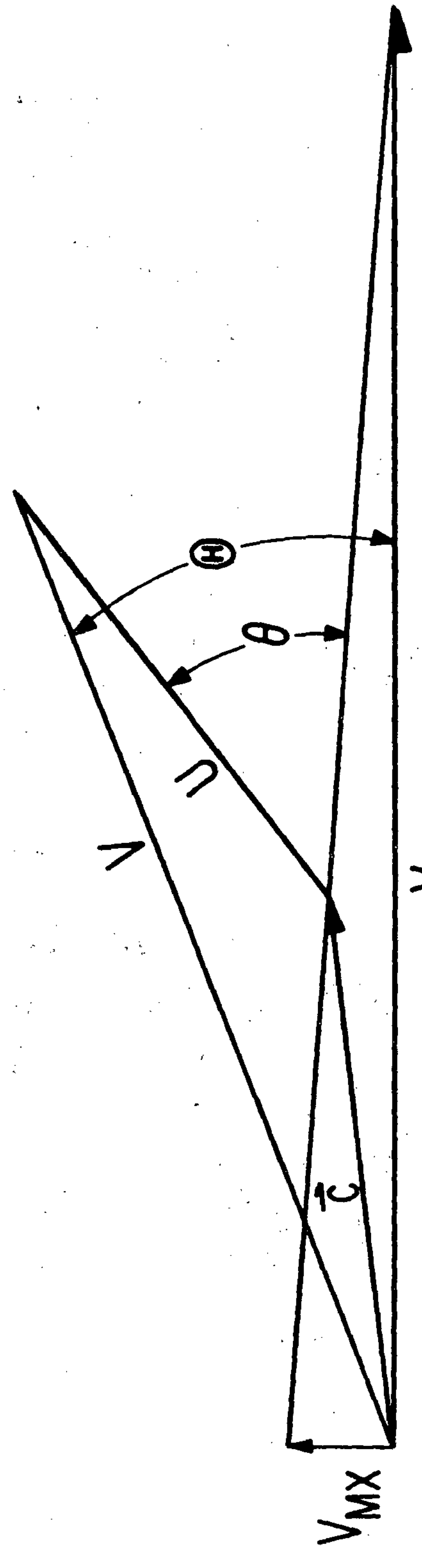

XBL 802-7976

Fig. 3

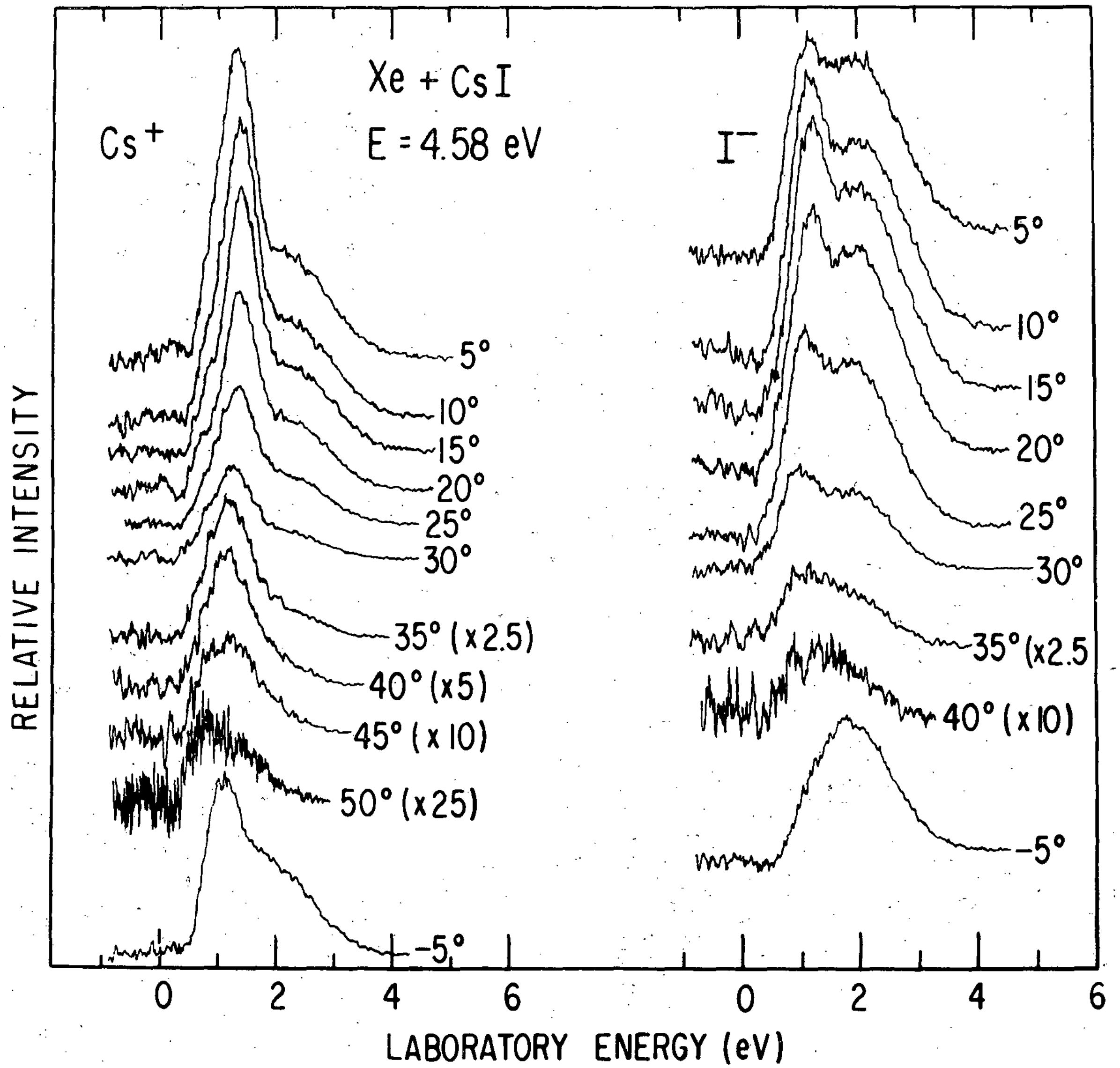

XBL 802-7977

Fig. 4

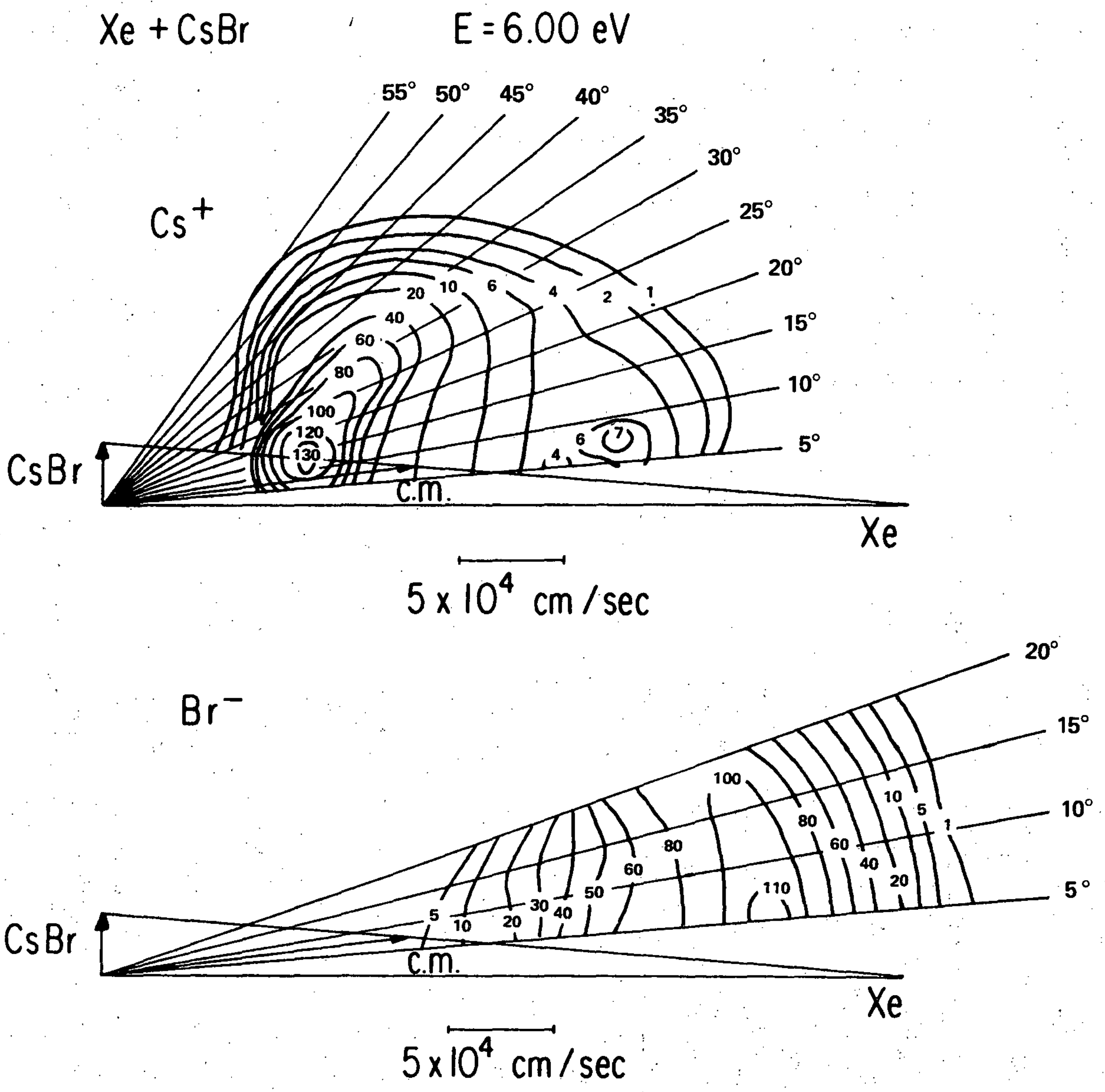

XBL 802-7978

Fig. 5

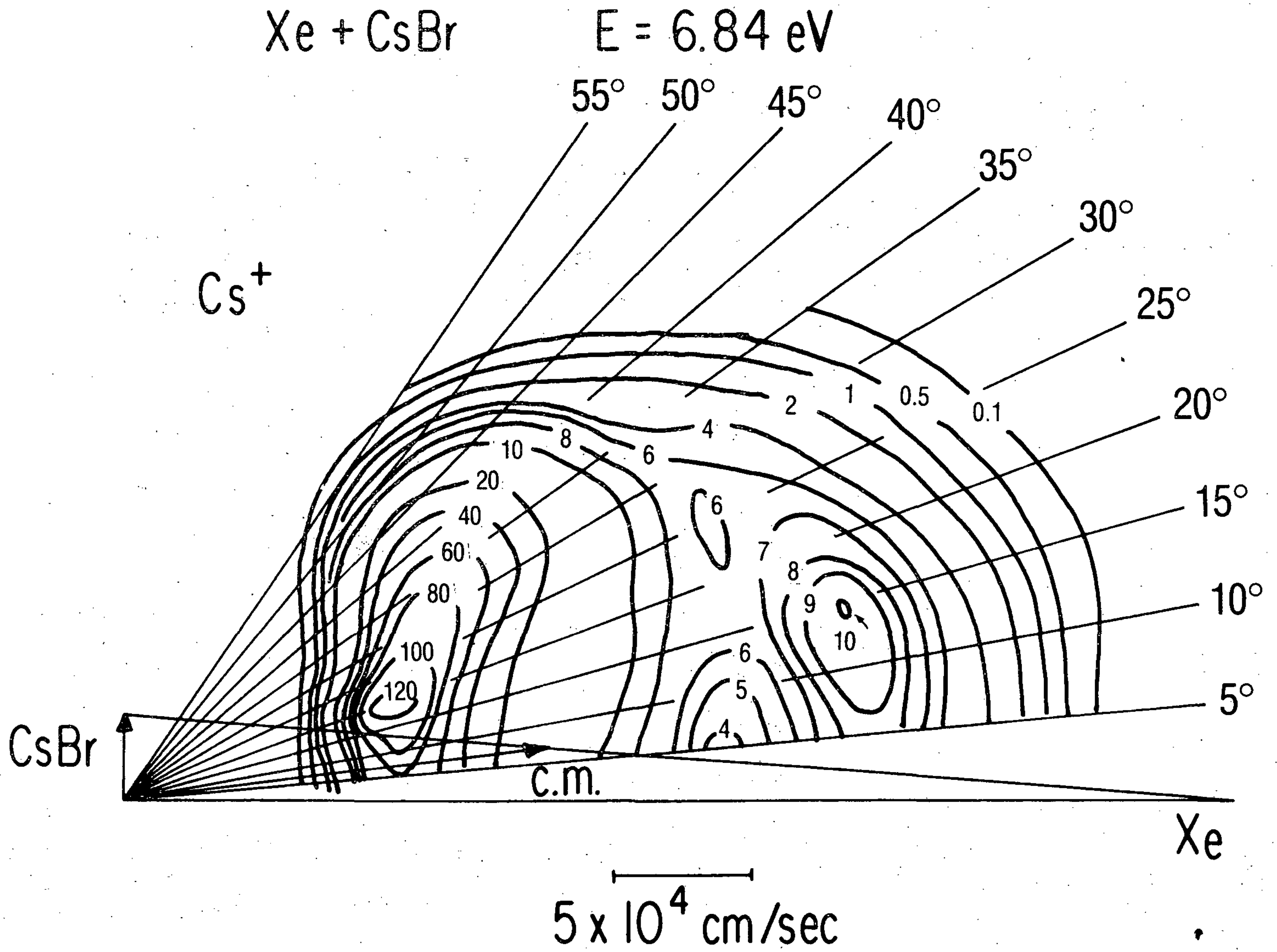

XBL 802-7979

Fig. 6

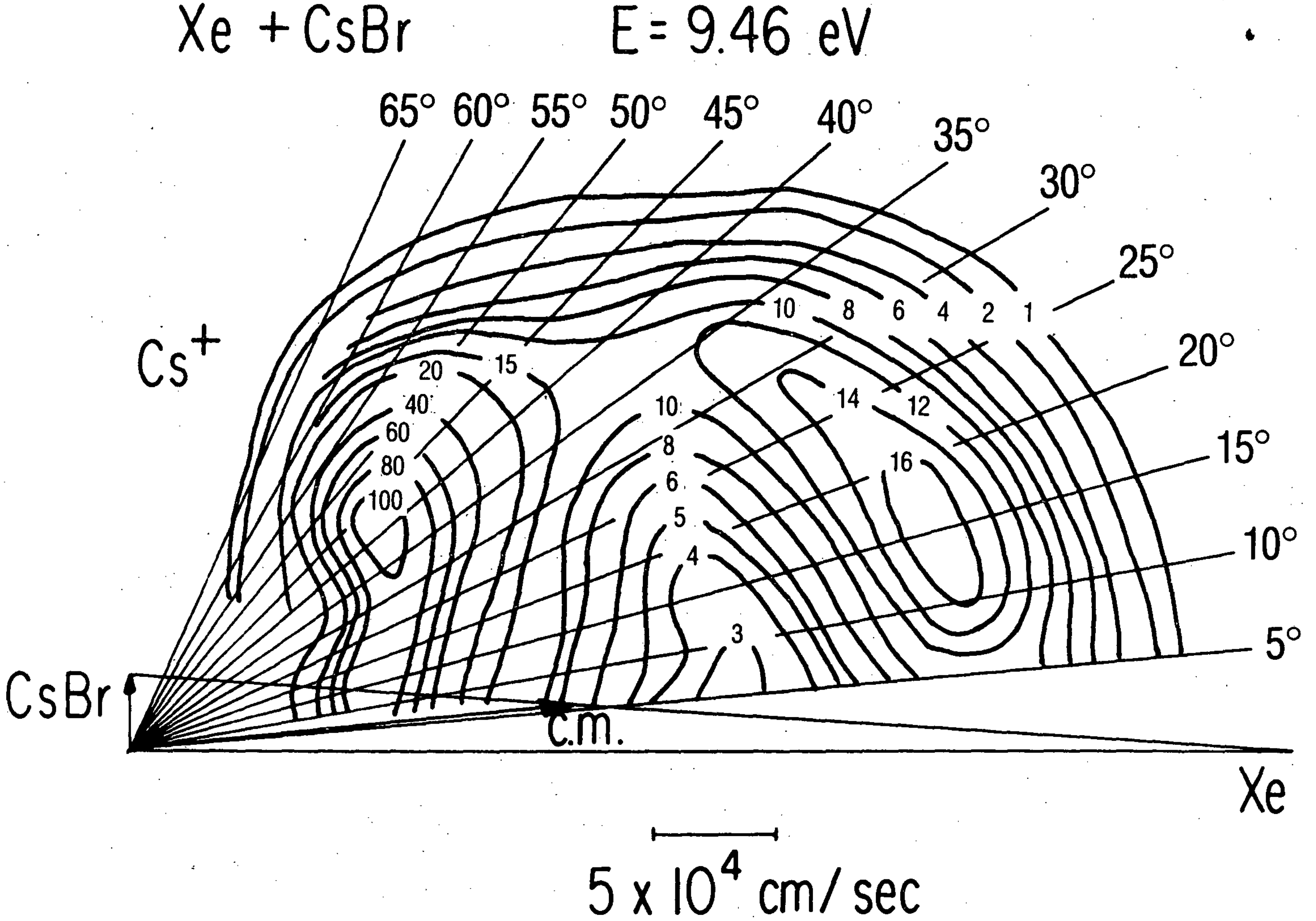

XBL 802-7980

Fig. 7

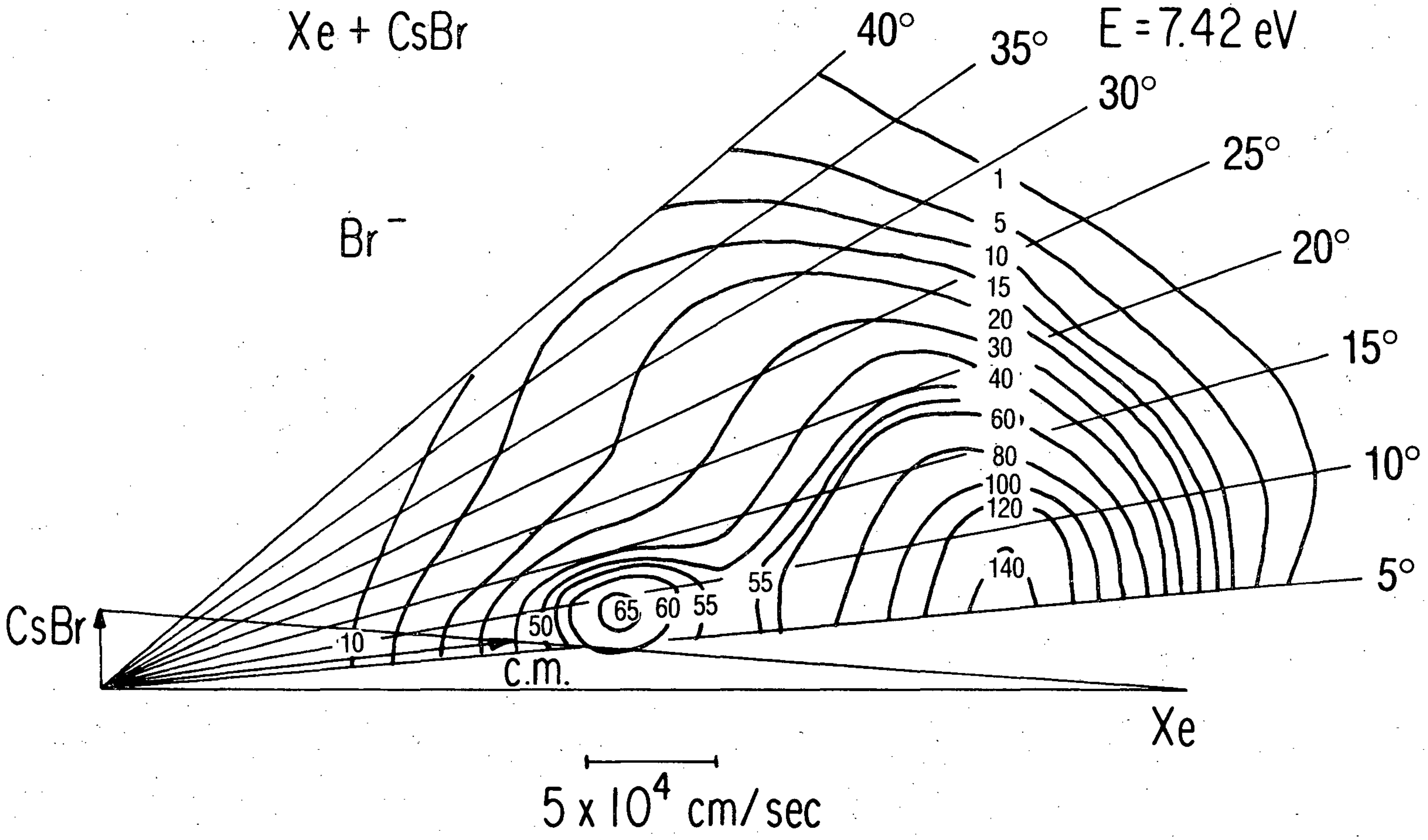

XBL 802-7981

Fig. 8

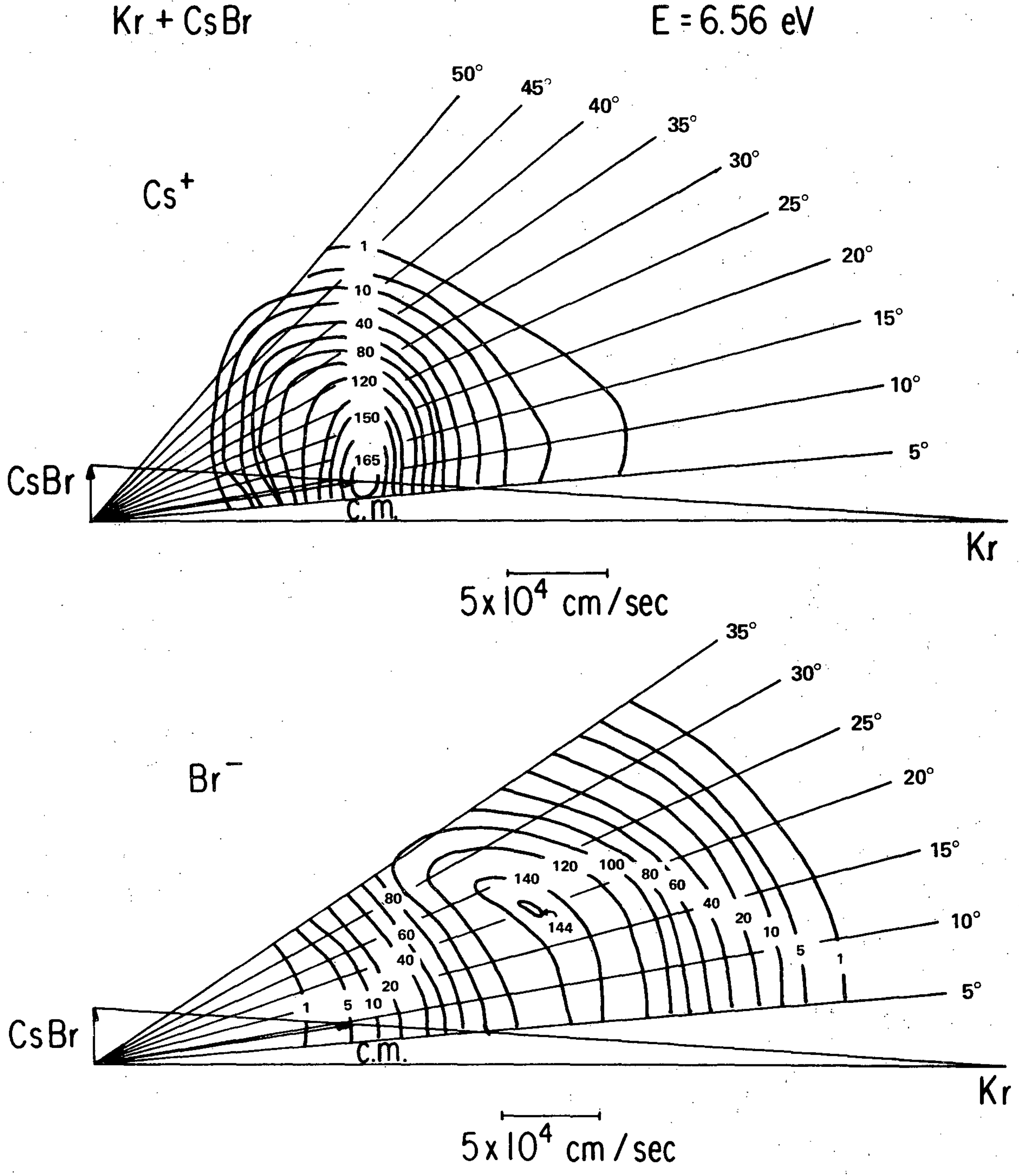

XBL 802-7982

Fig. 9

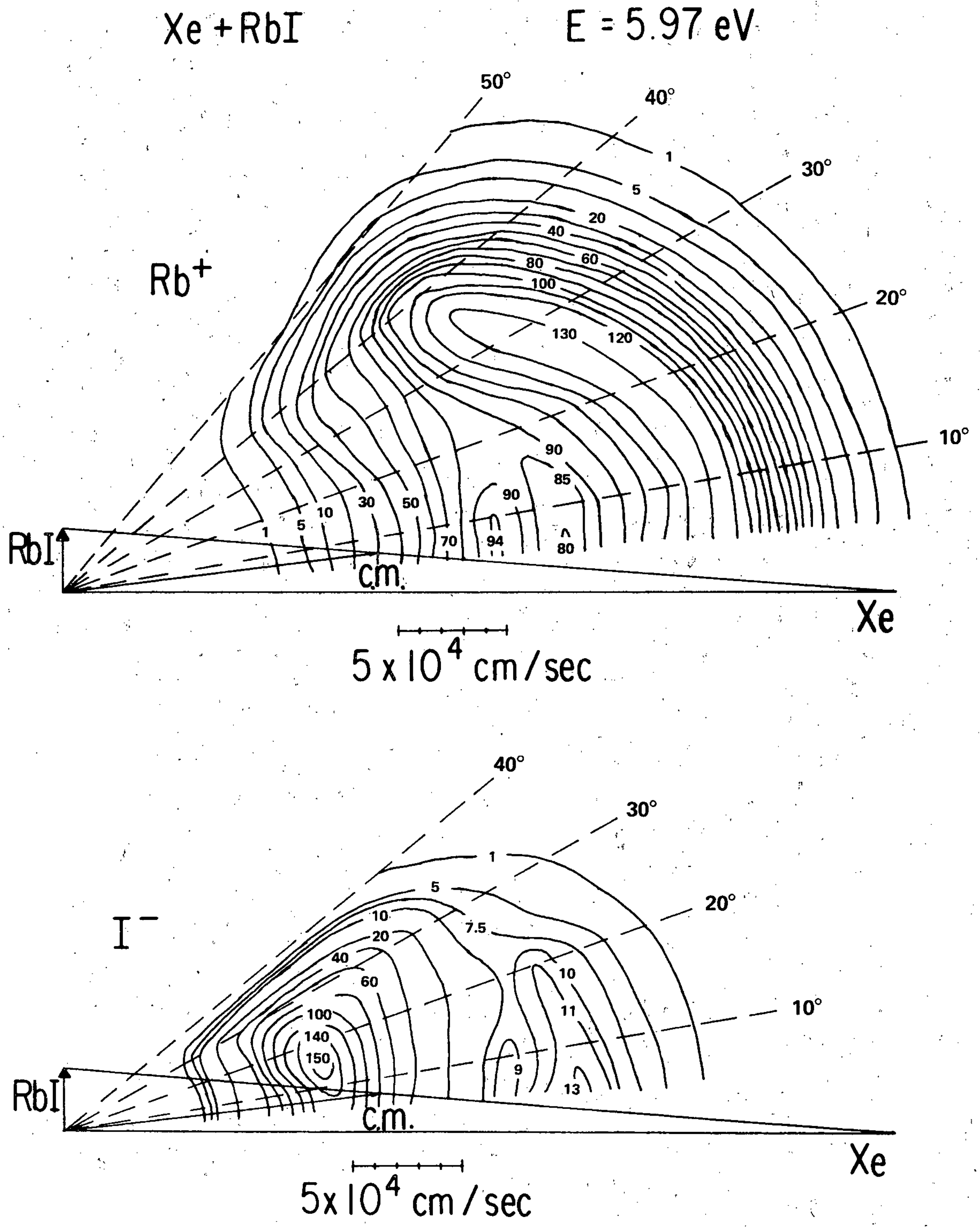

XBL 802-7983

Fig. 10

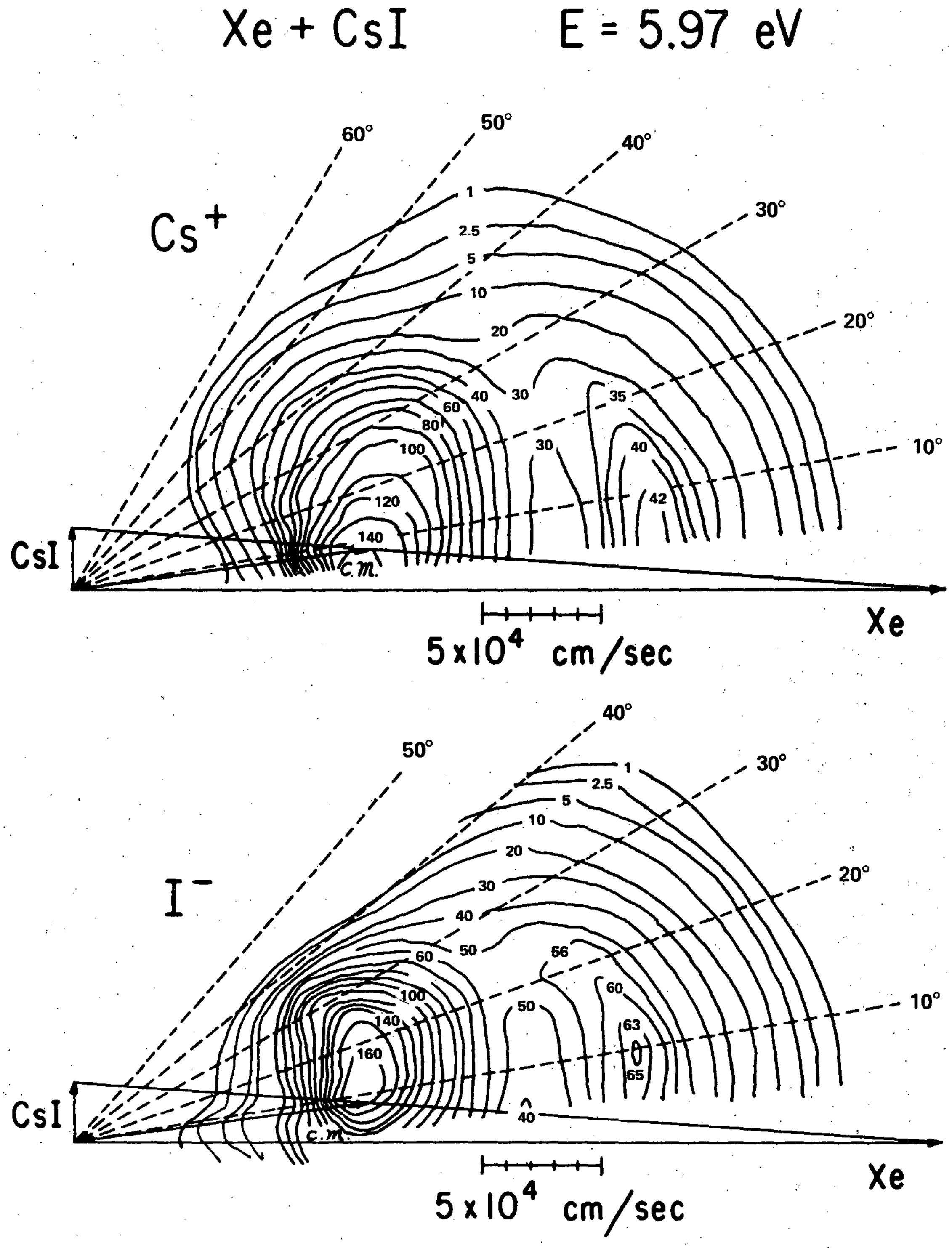

XBL 802-7984

Fig. 11

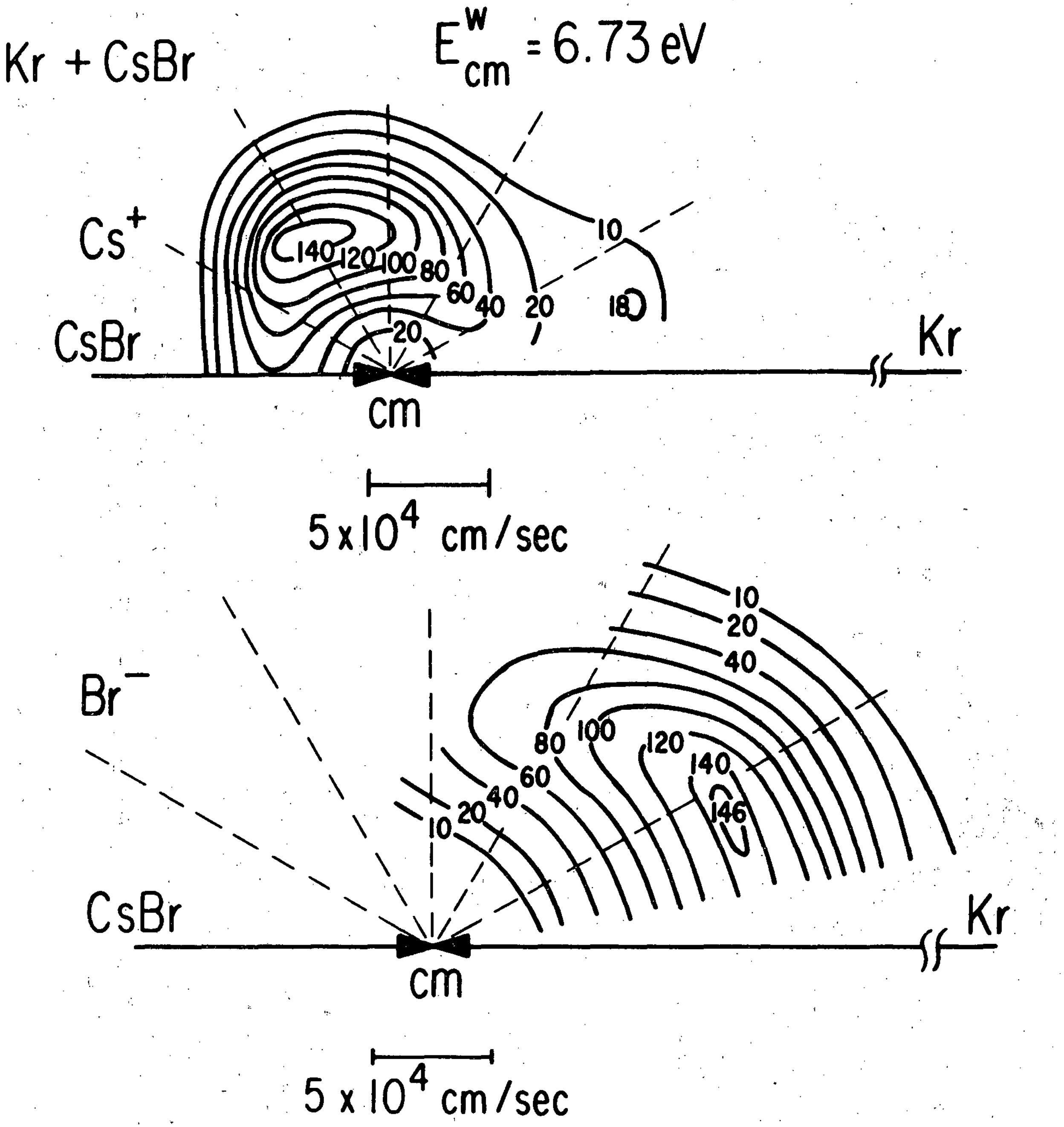

XBL 802-7985

Fig. 12

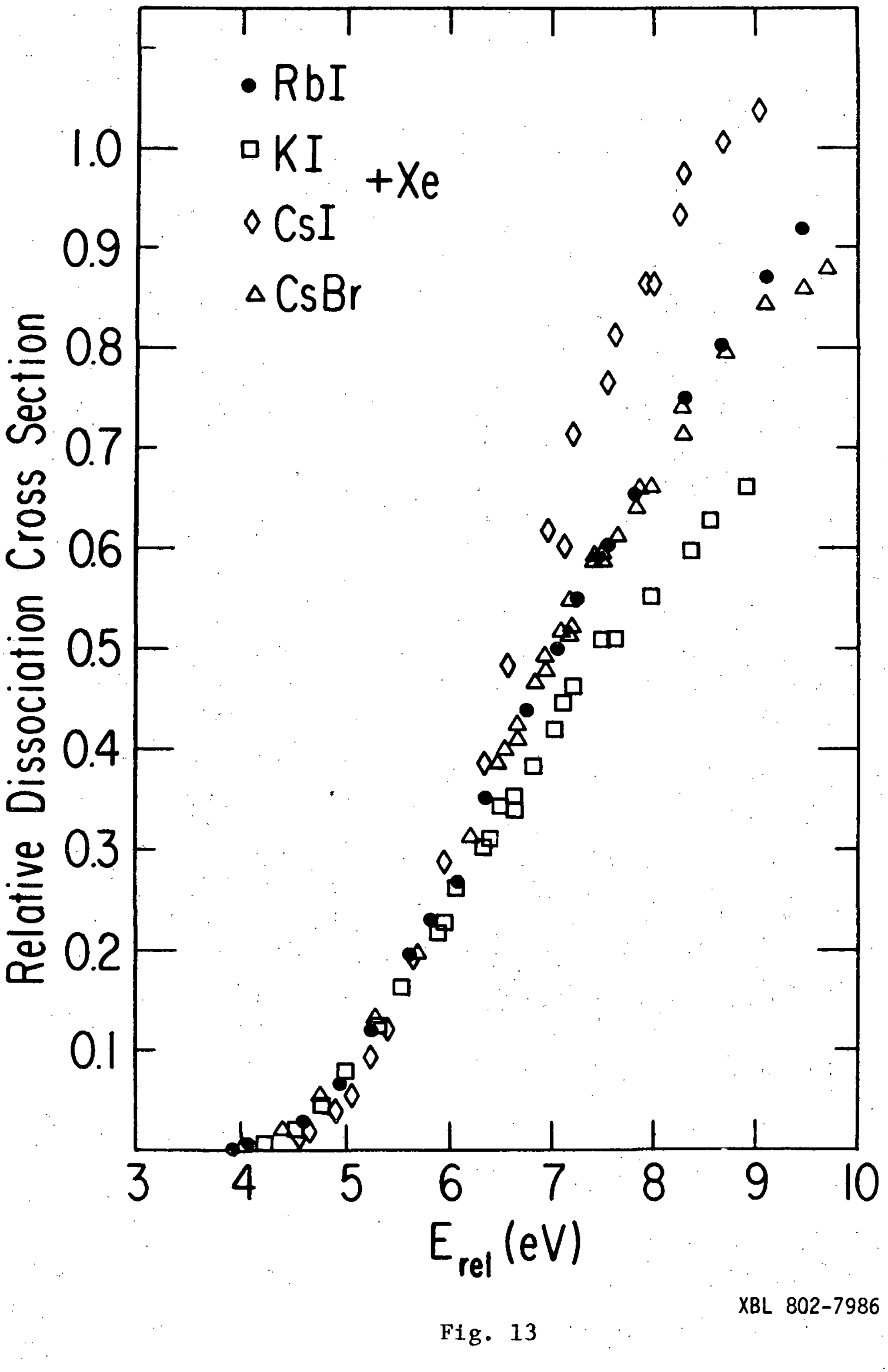

XBL 802-7986

Fig. 13

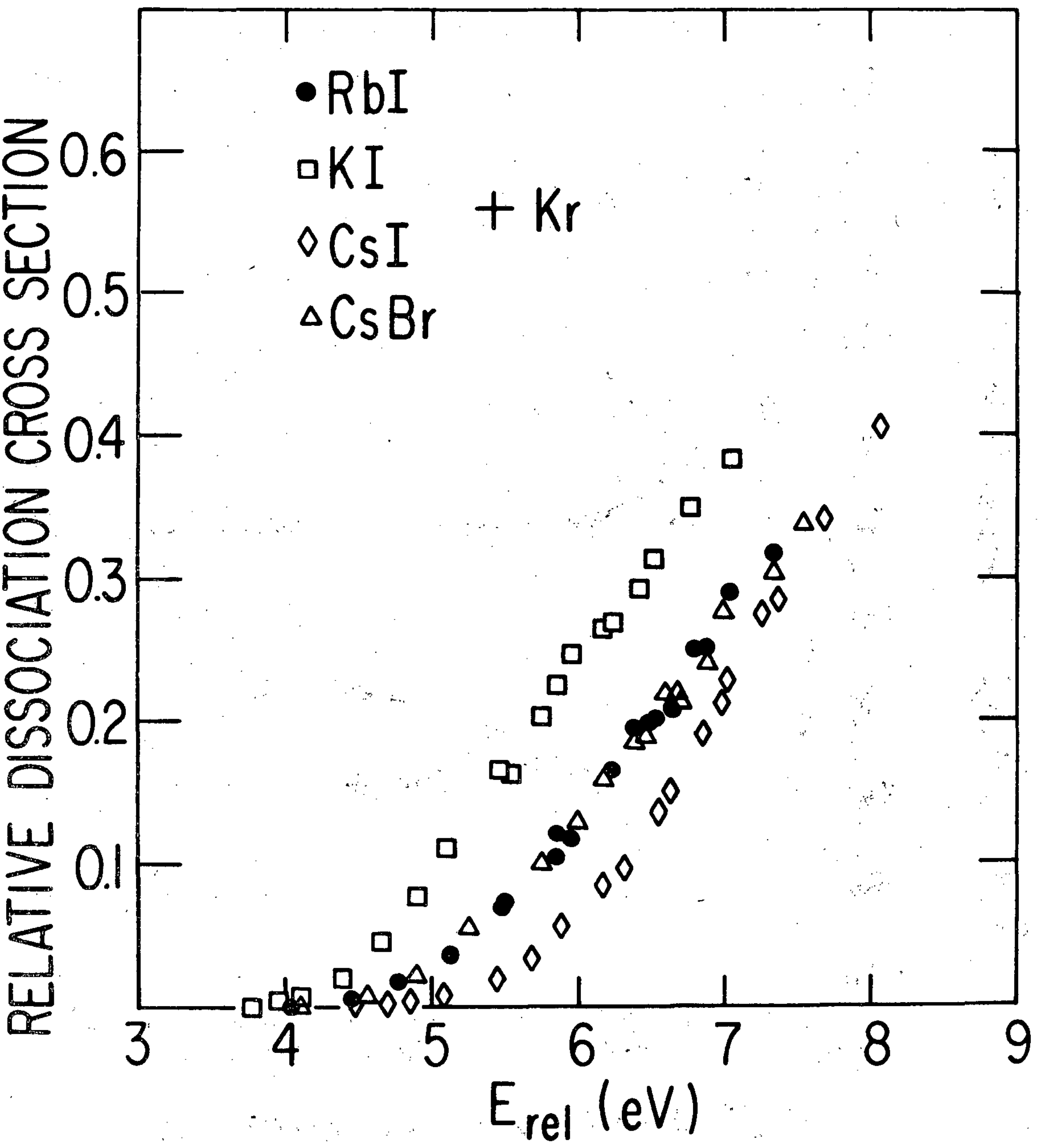

XBL 802-7987

Fig. 14

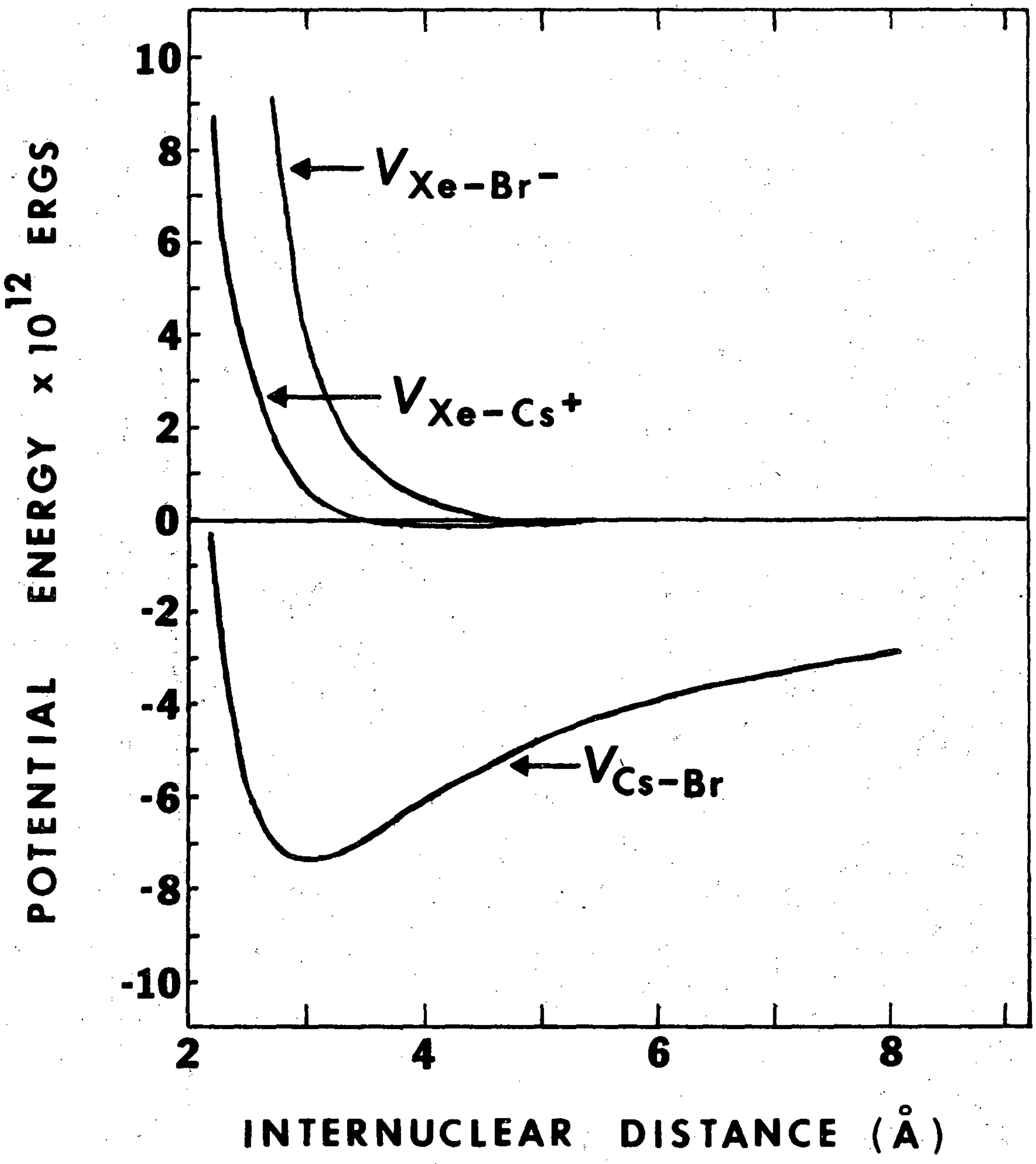

XBL 802-7988

Fig. 15

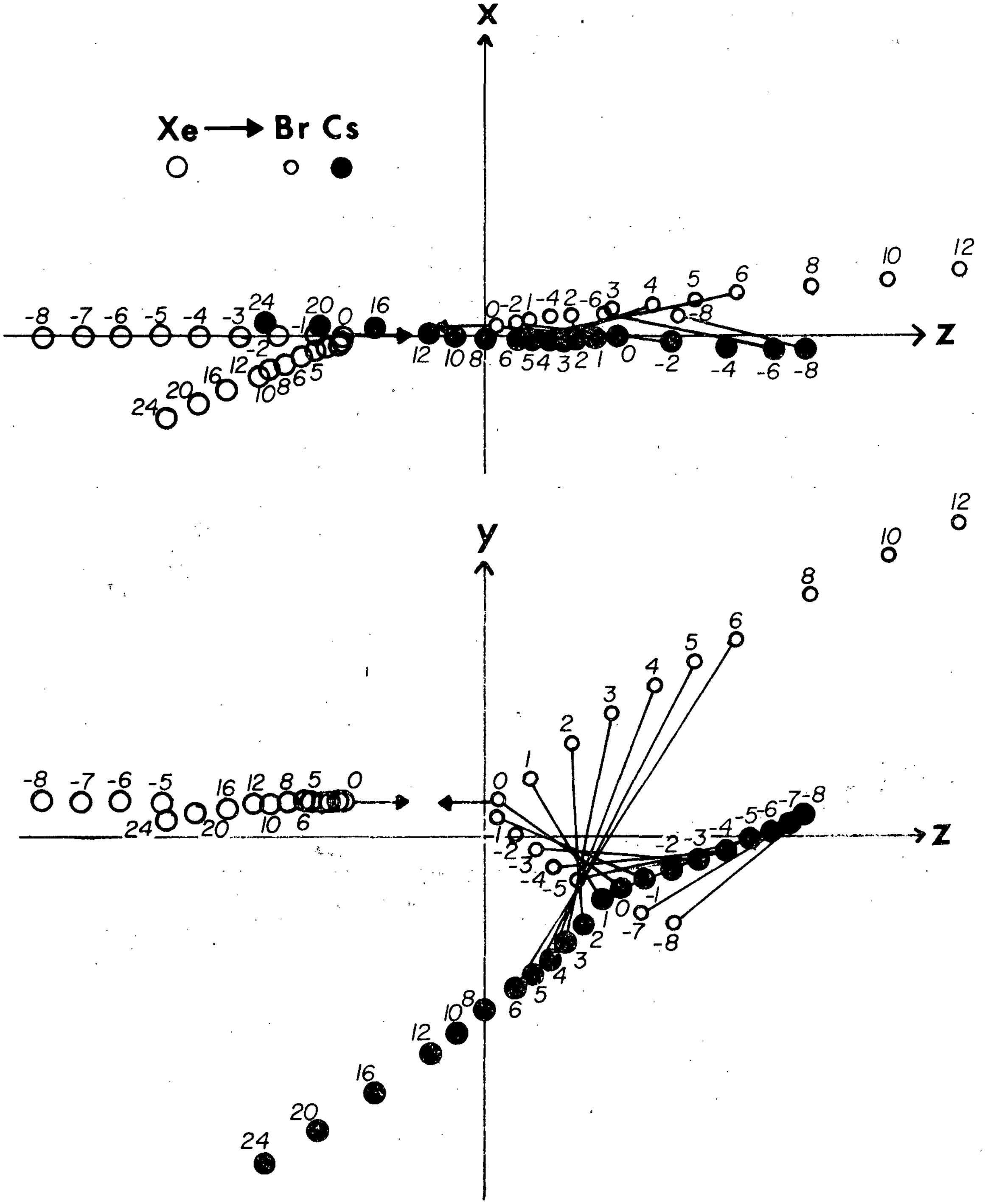

XBL 802-7989

Fig. 16

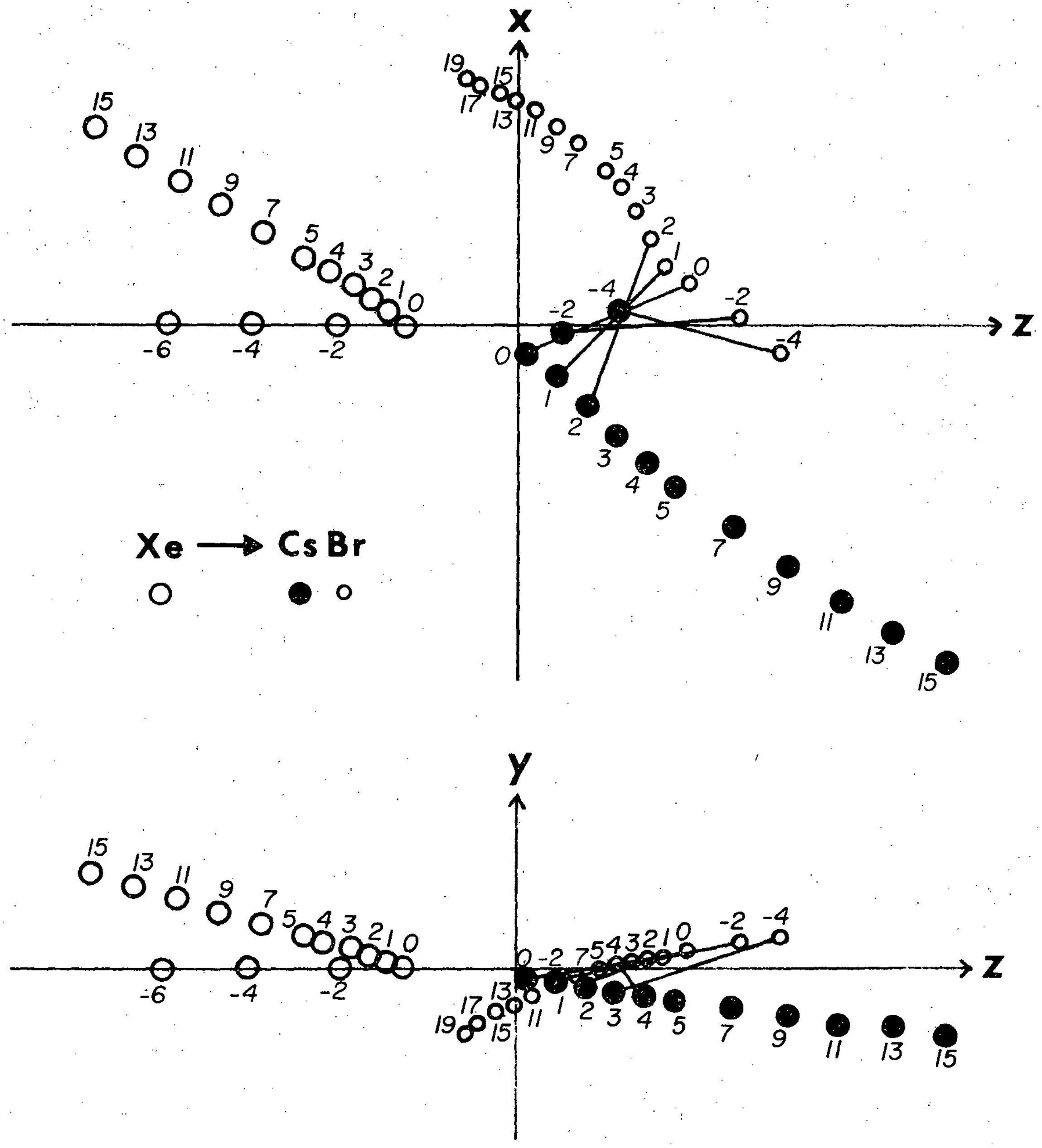

XBL 802-7990

Fig. 17

TECHNICAL INFORMATION DEPARTMENT
LAWRENCE BERKELEY LABORATORY
UNIVERSITY OF CALIFORNIA
BERKELEY, CALIFORNIA 94720